Secular and orbital-scale variability of equatorial Indian Ocean summer monsoon winds during the late Miocene

Clara T. Bolton, Emmeline Gray, Wolfgang Kuhnt, Ann E. Holbourn, Julia Lübbers, Katharine Grant, Tachikawa Kazuyo, Gianluca Marino, Eelco J. Rohling, Anta-Clarisse Sarr, et al.

Clim. Past, 18, 713–738, 2022
https://doi.org/10.5194/cp-18-713-2022

Climate of the Past
Open Access
EGU

Secular and orbital-scale variability of equatorial Indian Ocean summer monsoon winds during the late Miocene

Clara T. Bolton[1], Emmeline Gray[1,a], Wolfgang Kuhnt[2], Ann E. Holbourn[2], Julia Lübbers[2], Katharine Grant[3], Kazuyo Tachikawa[1], Gianluca Marino[3,4], Eelco J. Rohling[3,5], Anta-Clarisse Sarr[1], and Nils Andersen[6]

[1]Aix Marseille Univ, CNRS, IRD, INRAE, Coll France, CEREGE, Aix-en-Provence, 13545, Aix-en-Provence, France
[2]Institute of Geosciences, University of Kiel, 24118 Kiel, Germany
[3]Research School of Earth Sciences, Australian National University, Canberra ACT 2601, Australia
[4]Centro de Investigación Mariña, Universidade de Vigo, GEOMA, Palaeoclimatology Lab, Vigo, 36310, Spain
[5]Ocean and Earth Science, University of Southampton, Southampton SO14 3ZH, UK
[6]Leibniz Laboratory for Radiometric Dating and Stable Isotope Research, University of Kiel, 24118 Kiel, Germany
[a]now at: School of Environment, Earth and Ecosystem Sciences, The Open University, Milton Keynes MK7 6AA, UK

Correspondence: Clara T. Bolton (bolton@cerege.fr)

Received: 24 June 2021 – Discussion started: 29 June 2021
Revised: 25 October 2021 – Accepted: 9 March 2022 – Published: 8 April 2022

Abstract. In the modern northern Indian Ocean, biological productivity is intimately linked to near-surface oceanographic dynamics forced by the South Asian, or Indian, monsoon. In the late Pleistocene, this strong seasonal signal is transferred to the sedimentary record in the form of strong variance in the precession band (19–23 kyr), because precession dominates low-latitude insolation variations and drives seasonal contrast in oceanographic conditions. In addition, internal climate system feedbacks (e.g. ice-sheet albedo, carbon cycle, topography) play a key role in monsoon variability. Little is known about orbital-scale monsoon variability in the pre-Pleistocene, when atmospheric CO_2 levels and global temperatures were higher. In addition, many questions remain open regarding the timing of the initiation and intensification of the South Asian monsoon during the Miocene, an interval of significant global climate change that culminated in bipolar glaciation. Here, we present new high-resolution (< 1 kyr) records of export productivity and sediment accumulation from International Ocean Discovery Program Site U1443 in the southernmost part of the Bay of Bengal spanning the late Miocene (9 to 5 million years ago). Underpinned by a new orbitally tuned benthic isotope stratigraphy, we use X-ray fluorescence-derived biogenic barium variations to discern productivity trends and rhythms. Results show strong eccentricity-modulated precession-band productivity variations throughout the late Miocene, interpreted to reflect insolation forcing of summer monsoon wind strength in the equatorial Indian Ocean. On long timescales, our data support the interpretation that South Asian monsoon winds were already established by 9 Ma in the equatorial sector of the Indian Ocean, with no apparent intensification over the latest Miocene.

1 Introduction

The Asian monsoon is a major hydrological phenomenon that is driven by atmospheric pressure gradients created by asymmetric heating between the equatorial Indian and western Pacific Oceans and the Indo-Asian landmass, creating strong seasonally reversing winds and ocean currents and heavy boreal summer precipitation over the Bay of Bengal and Indian subcontinent (Webster, 1987a, b; Schott and Mccreary, 2001; Gadgil, 2003; Schott et al., 2009). Surface winds over the northern Indian Ocean (Arabian Sea and Bay of Bengal) and South China Sea are strong indicators of the strength of the South Asian and East Asian monsoon subsystems, respectively, and precipitation amount and seasonality can also be diagnostic of monsoon strength (e.g. Webster and Yang, 1992; Goswami et al., 1999). Thus, past monsoon dynamics can be reconstructed using wind, runoff, and precipitation indicators recorded in marine sediments from these core convective regions in the Bay of Bengal and South

China Sea. The Asian monsoon is known to have varied substantially over short (interannual to suborbital) and long (orbital to geological) timescales in response to forcing factors both external and internal to Earth's climate system (e.g. Wang et al., 2005; Clemens and Prell, 2003; Farnsworth et al., 2019; Kathayat et al., 2016).

There is great uncertainty surrounding the timing of Asian monsoon initiation and intensification, and the degree of coupling between regional monsoon subsystems. Discrepancies in part stem from the fact that records come from the South Asian or East Asian monsoon subsystems, which are sensitive to different aspects of regional topography (Molnar et al., 2010; Clift et al., 2008; Clift and Webb, 2019; Boos and Kuang, 2010; Acosta and Huber, 2020). Further, differences in monsoon expression occur even within the core convective region of the South Asian monsoon (e.g. dominance of summer monsoon winds in the southern Bay of Bengal vs. monsoonal rainfall–runoff in the northern and eastern parts). Meanwhile, proxies generally record singular aspects of monsoonal climate that are not necessarily coupled on all timescales (e.g. winter or summer monsoon winds, precipitation total amount, or degree of seasonality). Evidence for strong monsoonal climates (i.e. with strong seasonality of precipitation) exists across Asia during the Paleogene (Spicer et al., 2017; Licht et al., 2014), yet many terrestrial records from southeast Asia suggest an onset of the monsoon near the Oligocene–Miocene boundary ($\sim$ 24–22 Ma) (Guo et al., 2002; Sun and Wang, 2005; Wang et al., 2005). Marine records of drift sedimentation near the Maldives archipelago as well as upwelling and oxygenation indicators from the Arabian Sea, both influenced by wind and surface ocean circulation, suggest an onset of strong seasonally reversing South Asian (monsoon) winds and Arabian Sea upwelling during the late middle Miocene ($\sim$ 13–10 Ma) (Zhuang et al., 2017; Gupta et al., 2015; Betzler et al., 2016, 2018; Bialik et al., 2020; Nigrini, 1991).

In contrast, a time interval in which records from different regions and proxies converge somewhat is the late Miocene. Magnetic records from the Chinese Loess Plateau are interpreted to show a long-term intensification of the East Asian summer monsoon (EASM) from $\sim$ 8.2 to 2.6 Ma (Ao et al., 2016). A late Miocene strengthening of Asian winter monsoons is inferred from South China Sea (Holbourn et al., 2018; Jia et al., 2003; Wan et al., 2007) and Andaman Sea (Lee et al., 2020) records. In the Arabian Sea, an intensification of upwelling and productivity at $\sim$ 8 Ma is interpreted to reflect a strengthening of the South Asian summer monsoon (SASM) (Kroon et al., 1991; Singh and Gupta, 2014; Gupta et al., 2004), although other studies find evidence contrary to this (Tripathi et al., 2017; Huang et al., 2007). Proposed monsoon intensifications during the late Miocene roughly coincide with strong global cooling (Herbert et al., 2016), and a number of studies have implicated cooling and the ramp-up of Antarctic glaciation in monsoon strengthening (Ao et al., 2016; Holbourn et al., 2018; Gupta et al., 2004). Until now, a lack of continuous, well-preserved marine sequences from the South Asian monsoon region has stalled our understanding of its complex evolution during the Miocene.

The SASM is thought to have varied strongly on orbital timescales because monsoon strength responds, both directly and via internal feedback mechanisms, to insolation forcing. Model simulations predict a stronger South Asian monsoon during summer insolation maxima at both precession minima and (to a lesser degree) obliquity maxima (Bosmans et al., 2018; Prell and Kutzbach, 1992, 1987; Kutzbach, 1981; Jalihal et al., 2019; Tabor et al., 2018; Ding et al., 2021). Precession is the dominant control on insolation and its seasonal distribution near the Equator, and proxy-based Pleistocene SASM records show strong precession-band (19–23 kyr) variability (Kathayat et al., 2016; Prell and Kutzbach, 1987; Clemens et al., 1991; Zhisheng et al., 2011; Bolton et al., 2013; Caley et al., 2011; Gebregiorgis et al., 2018; Wang et al., 2005; Clemens and Prell, 1990; Rostek et al., 1997). The influence of global boundary conditions related to global ice volume and greenhouse gas concentrations on SASM winds and precipitation–runoff is also demonstrated by strong obliquity- and eccentricity-band variance in Plio-Pleistocene records (e.g. Clemens and Prell, 2003; Gebregiorgis et al., 2018; Clemens et al., 2021; An et al., 2011). Our current knowledge of orbital-resolution past productivity fluctuations in the South Asian monsoon region and their relationship with local (insolation) or remote (global ice volume, greenhouse gases) forcing mechanisms comes almost entirely from Pleistocene Arabian Sea sedimentary records (Clemens and Prell, 2003; Caley et al., 2011; Singh et al., 2011; Shimmield and Mowbray, 1991; Rogalla and Andruleit, 2005; Clemens et al., 1991; Ziegler et al., 2010). These records suggest that summer monsoon proxies significantly lag Northern Hemisphere summer insolation maxima in the precession and obliquity bands due to climate feedbacks. Orbital control on past SASM strength in the pre-Pleistocene, when boundary conditions were different, has so far only been investigated in the Andaman Sea over the latest Miocene–early Pliocene, where seawater oxygen isotope data suggest high-amplitude precession and obliquity forcing of monsoon rainfall with significant phase lags (Jöhnck et al., 2020).

In this paper, we investigate sediment accumulation and export productivity dynamics at millennial resolution in late Miocene sediments from the southern Bay of Bengal (BOB) International Ocean Discovery Program (IODP) Site U1443 (5°23′ N, 90°22′ E, Fig. 1). The late Miocene (11.6–5.3 Ma) is an interval of major global climate change, with long-term cooling between $\sim$ 7.5 and 5.5 Ma (Herbert et al., 2016) culminating in major high-latitude cooling events (Holbourn et al., 2018), and important carbon cycle shifts recorded in the marine and terrestrial realms potentially linked to atmospheric CO_2 decline (Tauxe and Feakins, 2020; Steinthorsdottir et al., 2021; Rae et al., 2021). The region of Site U1443 is strongly influenced by seasonally reversing mon-

soon winds today, and primary productivity is tightly coupled to the annual monsoon cycle (Figs. 1a–b, 2). During the SASM, strong moisture-laden winds blow inland, driving surface circulation changes and increased mixed layer depth (Fig. 1a–b) (Webster, 1987a, b; Schott and Mccreary, 2001; Gadgil, 2003; Schott et al., 2009). Strong Ekman pumping mixes nutrients into the surface layer during the South Asian summer monsoon and, to a lesser extent, the winter monsoon, stimulating biological productivity (Fig. 2) (Lévy et al., 2007; Mccreary et al., 2009; Koné et al., 2009; Behrenfeld et al., 2005; Longhurst, 1995). This strong seasonal signal is transferred to the sedimentary record in the form of strong variance at orbital periods because insolation variations drive seasonal contrast. Here, we generate a new orbitally tuned age model based on benthic foraminiferal stable isotopes spanning ∼ 9 to 5 Ma. Core-scanning X-ray fluorescence (XRF) data are then used to reconstruct bulk, carbonate, and biogenic barium content and mass accumulation rates (MARs), shedding light on secular and orbital-scale export productivity and sedimentation changes over the late Miocene.

2 Background

In the modern southern BOB waters overlying Site U1443, both primary and export productivity are strongly controlled by seasonally reversing winds associated with the South Asian monsoon. Figure 2 shows the annual cycle of wind stress, mixed layer depth (MLD), net primary productivity, and biogenic particle export based on recent oceanographic, satellite, and sediment trap data (see Sect. 3.2 for details). In boreal summer (June, July, and August: JJA) strong southwest winds mix the upper water column, deepening the MLD to ∼ 60 m and entraining nutrients into the photic zone, leading to enhanced primary productivity and biogenic particle export (with a lag of ∼ 3–4 weeks) (Figs. 1a–b, 2). During boreal winter, northeast winds deepen the MLD to a lesser extent, resulting in a second smaller peak in productivity during the winter monsoon (December, January, and February: DJF) (Fig. 2). During the inter-monsoon seasons, lowest wind stress is recorded leading to a shallow MLD, higher sea surface temperatures (SSTs), and a more stratified upper water column, resulting in increased oligotrophy and reduced biological productivity. The biannual productivity maxima observed in the surface ocean above Site U1443 are characteristic of monsoon-dominated tropical regions (Longhurst, 1995; Lévy et al., 2007).

Sediment trap data suggest that primary productivity is the dominant control on organic carbon export at a location west of the northern end of the Ninetyeast Ridge (Southern Bay of Bengal Trap Station (SBBT) site; 5° N, 87° E, Fig. 1c). However, lithogenic mineral ballasting at this location is not negligible (average ∼ 13 % and 15 % lithogenic particles in shallow and deep traps respectively) (Rixen et al., 2019;

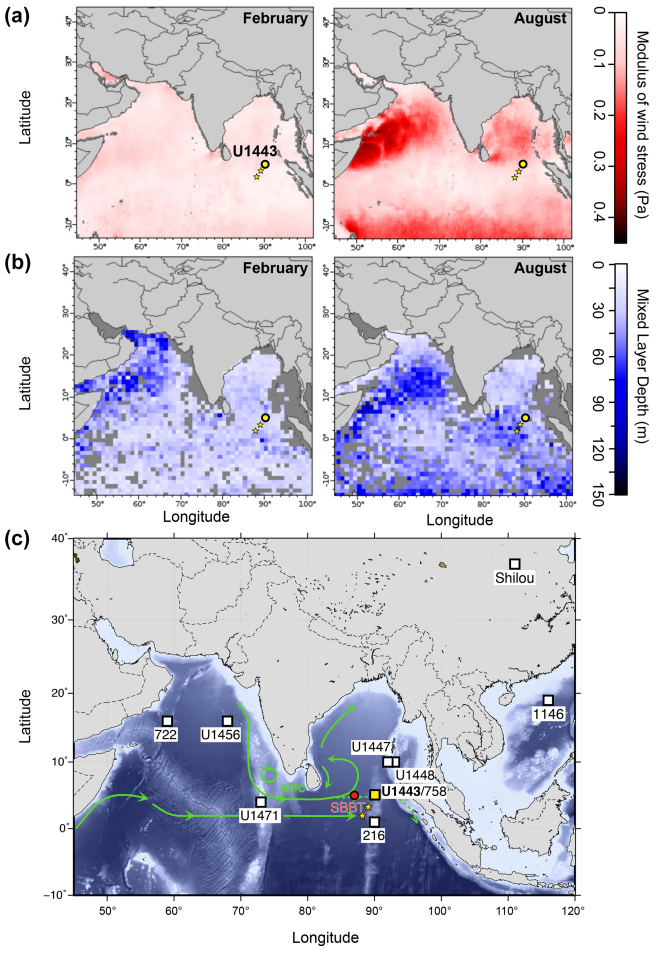

Figure 1. Seasonal contrast (February vs. August) in wind stress **(a)** and mixed layer depth **(b)**. Yellow dots indicate the modern position of IODP Site U1443, and yellow stars its paleo-position at 9 Ma (1.71° N, 88.06° E) and 5 Ma (3.27° N, 89.04° E) calculated using GPlates: http://portal.gplates.org/service/reconstruct_points (last access: 1 September 2021). Maps were created on the ERDDAP website using the datasets *Wind Stress, Metop-A ASCAT, 0.25°, Global, Near Real Time, 2009-present (Monthly)* and *Ocean Climatology Ocean Mixed Layer Depth MLD T02 kriging* (see Sect. 3.2 for details). **(c)** Regional bathymetric map showing modern locations of marine and terrestrial sites discussed in this study (white squares) and the position of Site U1443, a redrill of Site 758, in the modern ocean (yellow square) and its paleo-position at 9 and 5 Ma (yellow stars). The red circle shows the location of the SBBT sediment trap. Green arrows show surface ocean circulation during the summer monsoon (July–August) and the eastward flow of waters from the Arabian Sea into the BOB via the Southwest Monsoon Current (SMC), after Schott et al. (2009).

Unger et al., 2003) and could in part explain the bias towards the late summer peak seen in biogenic fluxes compared to net primary productivity, as maximum concentrations of lithogenic particles at SBBT occur during the summer monsoon. While wind forcing is identified as the dominant factor controlling biogenic particle fluxes at the SBBT site, ad-

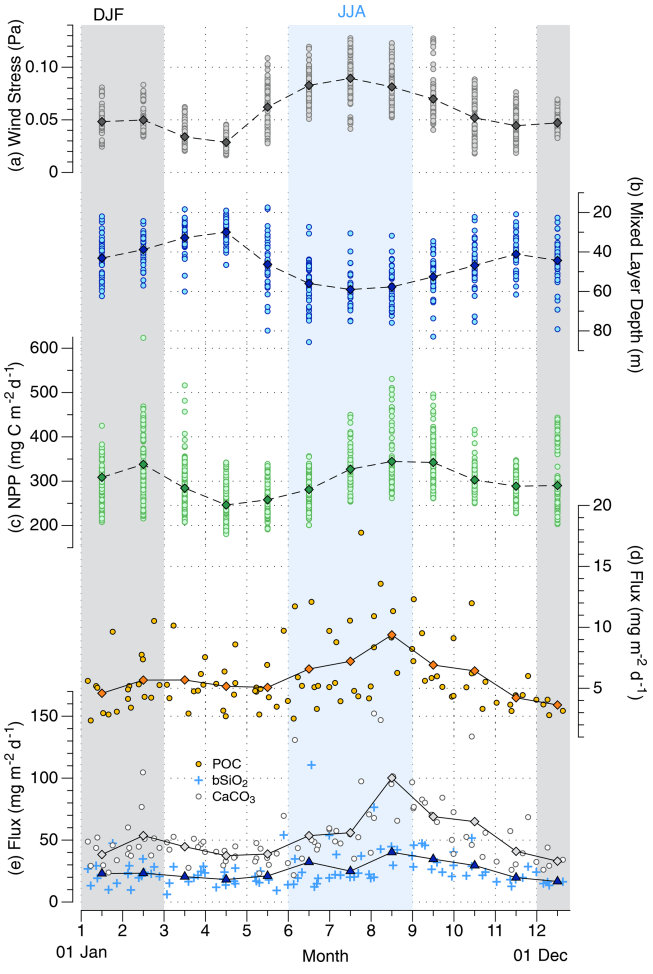

Figure 2. Modern, seasonal oceanographic variability above Site U1443 in the southern BOB. **(a)** Wind stress, **(b)** mixed layer depth (MLD), **(c)** net primary productivity (NPP), **(d)** particulate organic carbon (POC) flux, and **(e)** biogenic silica (bSi) and calcium carbonate ($CaCO_3$) flux. See Sect. 3.1 for details of individual datasets and sources. Points represent individual months; diamonds and triangles with lines represent monthly mean values over entire time series. Months (x axis) run from 1 (1 January) to 12 (1 December). JJA: June, July, August; DJF: December, January, February.

vection of nutrient- and chlorophyll-rich waters originating from the eastern Arabian Sea via the Southwest Monsoon Current may further contribute to the summer productivity peak in this region (Unger et al., 2003). During the summer monsoon, the relatively salty and nutrient-rich Southwest Monsoon Current flows eastwards south of Sri Lanka then turns northwards into the BOB (Fig. 1c) (Schott et al., 2009; Jensen, 2003). The Southwest Monsoon Current and associated eddies have been shown to increase chlorophyll concentrations and average phytoplankton size along their paths as far east as 88–90° E, with the current's influence generally restricted to north of 6° N at this longitude (Jyothibabu et al., 2015; Vinayachandran et al., 2004; Webber et al., 2018). While river runoff and resultant salinity stratification during the summer monsoon suppress primary productivity further north in the BOB (Prasanna Kumar et al., 2002), seasonal surface salinity variations are very small (< 0.2 psu) at 5° N (Zweng et al., 2013). Accordingly, monsoon impacts on nutrients and productivity in our study area are limited to those driven by surface currents and wind mixing, and biogenic export fluxes during the SASM are similar (particulate organic carbon) or higher ($CaCO_3$ and biogenic SiO_2) than at sites further north in the BOB (Unger et al., 2003). Thus, modern data give us confidence that export productivity at our site is likely a reflection of South Asian (primarily summer) monsoon wind strength, via its control on MLD and nutrient entrainment into the mixed layer and surface ocean currents.

3 Materials and methods

3.1 Site and sampling

Samples used in this study are from Site U1443 (5°23.01′ N, 90°21.71′ E, water depth 2924 m), drilled during IODP Expedition 353 in the southernmost part of the BOB on the crest of Ninetyeast Ridge (NER) (Clemens et al., 2016) (Fig. 1). During the late Miocene, Site U1443 is estimated to have migrated northeastwards from 1°71′ N, 88°06′ E at 9 Ma to 3°27′ N, 89°04′ E at 5 Ma (Fig. 1; paleo-location estimates from http://portal.gplates.org, last access: 1 September 2021), although its position relative to peninsular India remained stable. Site U1443 is located ∼ 100 m southeast of Ocean Drilling Program (ODP) Site 758 and is a redrill of this legacy site (Shipboard Scientific Party, 1989). At Site U1443, the use of Advanced Piston Coring (APC) and half-length APC drilling techniques down to > 200 m CSF (core depth below sea floor) in three holes allowed recovery of a compete, spliced Neogene sedimentary section spanning 0–195 m CCSF (core composite depth below sea floor). Late Miocene records cover the interval 70.06 m CCSF (U1443B 7H 5W 75–76 cm) to 122.76 m CCSF (U1443C 15H 4W 148–149 cm), following the revised shipboard splice (Table S1 in the Supplement), spanning the interval ∼ 9.5 to 5 Ma based on initial bio-magnetostratigraphy. Samples come from lithologic Units Ib and IIa, and sediments mainly consist of light grey to pale yellow nannofossil ooze with clay and foraminifers, and occasional volcanic ash (Clemens et al., 2016). Cores were sampled (1 cm half rounds) at a depth resolution of 4 cm in the upper part of the late Miocene interval (70.06–114.18 m) and 2 cm in the lower part (114.18–122.76 m) where sedimentation rate estimates were lower. U-channels for XRF scanning were sampled from archive halves of sediment cores at Kochi Core Centre (Japan) during the post-cruise sampling party for 39 sections included in the splice between U1443C 9H 2A (69.95 m CCSF) and U1443C 13H 5A (113.58 m CCSF).

3.2 Modern oceanography

Modern oceanographic conditions over the seasonal cycle above Site U1443 were assessed using recent datasets to investigate the regional relationship between monsoon winds and biological productivity (Figs. 1a–b, 2). Monthly data for wind (wind stress, Metop-A ASCAT, 0.25°, global, near real time, 2009–present) (Fig. 2a), MLD (1969–2010) (Keerthi et al., 2013) (Fig. 2b), and depth-integrated net primary productivity estimated from satellite-derived surface chlorophyll concentrations (primary productivity, Aqua MODIS, NPP, global, 2003–present, experimental (monthly composite) calculated using the method of Behrenfeld and Falkowski, 1997, and ERD et al., 2020) (Fig. 2c) were extracted for a box between ∼ 4.5–5.5° N latitude and 89–91° E longitude (depending on grid resolution) and binned by month. Scatter thus reflects a combination of spatial variability within our 1° × 2° box and interannual variability; monthly means over each time series are also shown. Particulate organic carbon, biogenic SiO_2, and $CaCO_3$ fluxes (Fig. 2d, e) are from SBBT sediment trap samples (∼ 5° N, 87° E, Fig. 1c) (Unger et al., 2003). In Fig. 2 we show data from the deep traps (∼ 3000 m, ∼ 21 d sampling intervals) (Rixen et al., 2019), but seasonal patterns of biogenic particle flux are very similar in the shallow (∼ 1000 m) SBBT traps (Unger and Jennerjahn, 2009; Vidya et al., 2013). Data points show fluxes recorded in individual years (1987–1997, plotted against mid-time for the trap deployment), with monthly averages also shown. Monthly wind and net primary productivity data were downloaded from the ERDDAP server (https://coastwatch.pfeg.noaa.gov/erddap/index.html, last access: 28 September 2020) and Indian Ocean MLD data (Keerthi et al., 2013) from http://www.ifremer.fr/cerweb/deboyer/mld/Surface_Mixed_Layer_Depth.php (last access: 28 September 2020).

3.3 Late Miocene benthic foraminiferal stable isotope data

Bulk sediment samples were oven-dried at 50 °C, weighed, and washed over a 63 µm sieve in tap water at CEREGE (Centre Européen de Recherche et d'Enseignement des Géosciences de l'Environnement). The > 63 µm fraction was oven-dried at 50 °C on a filter paper and weighed to determine percentage coarse fraction. The < 63 µm fraction was centrifuged and dried at 50 °C. Depth resolution for the benthic isotope record is 8 cm (70.06 to 112.87 m CCSF), 4 cm (112.86 and 114.18 m CCSF), or 2 cm (114.18–122.76 m CCSF), except near splice tie points where sampling included overlap between cores increasing resolution. In total, 6 to 12 specimens of the epibenthic foraminiferal species *Cibicidoides wuellerstorfi* were picked from the > 212 µm fraction, with 6–8 well-preserved specimens selected for analysis. Tests were broken into fragments, cleaned in ethanol in an ultrasonic bath, and oven-dried at 40 °C. Stable carbon and oxygen isotopes were measured on a Thermo Scientific MAT 253 dual-inlet isotope ratio mass spectrometer (DI-IRMS) coupled to a Kiel IV carbonate preparation device at the Leibniz Laboratory, University of Kiel. Based on long-term analysis of international and internal carbonate standards, precision (1σ) is better than ±0.08 ‰ for $\delta^{18}O$ and 0.05 ‰ for $\delta^{13}C$. Results were calibrated using the National Institute of Standard and Technology (NIST) carbonate isotope standard NBS (National Bureau of Standard) 19 and are reported on the Vienna PeeDee Belemnite (VPDB) scale. *C. wuellerstorfi* isotope data below 112.86 m CCSF were originally published in Lübbers et al. (2019), and a low-resolution version of the long-term $\delta^{13}C$ record in Bretschneider et al. (2021).

3.4 Age model

Seven calcareous nannofossil bio-events dated between 9.53 and 5.04 Ma were identified at ∼ 0.5 to 1 m resolution in Site U1443 splice samples (Table S2) to increase the resolution of shipboard biostratigraphy (Robinson et al., 2016). To check for orbital periodicities prior to tuning, wavelet analyses were performed on benthic isotope records in the depth domain and on the revised nannofossil-based age model (using a fourth-order polynomial fit, Fig. S1 in the Supplement) in R using the biwavelet package (Gouhier et al., 2018; Grinsted et al., 2004) (Fig. S2a–d). All time series were first interpolated to constant depth or age resolution, such that the maximum resolution present was preserved (2 cm and 2 kyr for benthic isotope records in the depth and age domain, respectively). Records were then detrended to remove signals with periods longer than one-third of the length of the dataset using the "bandpass" function in the R package Astrochron (Meyers, 2014). Wavelets indicate that obliquity-driven cycles are present throughout (∼ 0.534 m, Fig. S2a–b; 41 and 53 kyr, Fig. S2c–d), confirming that the U1443 record is suitable for orbital tuning. Using revised nannofossil datums (Table S2, Fig. S1) and shipboard magnetostratigraphy (Clemens et al., 2016) as preliminary age–depth tie points (Fig. 3), an astronomical age model was constructed by tuning our monospecific benthic $\delta^{18}O$ record to an eccentricity plus tilt (ET) target curve (Laskar et al., 2004) (Table S3, Fig. 4). We did not include precession in our tuning target so as not to introduce assumptions related to which hemisphere was controlling climate at our site, and because the temporal resolution of our benthic record does not permit accurate resolution of precession cycles in some intervals. We used a minimal tuning approach, tying ET maxima to benthic $\delta^{18}O$ minima, with at most one tie point per ∼ 100 kyr and often one every 200–300 kyr (Figs. 4, S1), so as not to artificially introduce frequency modulations (Zeeden et al., 2015).

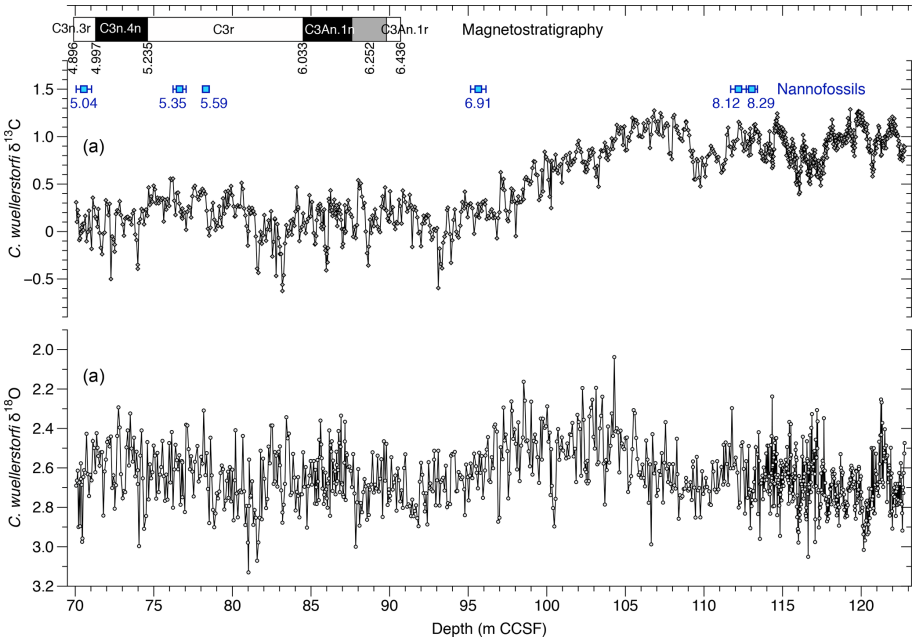

Figure 3. U1443 benthic foraminiferal (*Cibicidoides wuellerstorfi*) δ^{18}O **(b)** and δ^{13}C **(a)** data on the composite depth scale. Blue squares show refined depth ranges for calcareous nannofossil datums (see Table S2), and shipboard magnetostratigraphy is also shown for the interval over which it could be reliably determined. Between ∼ 90 and 128 m CCSF, sediments in cores from all holes showed scattered directional signals during pass-through magnetic remanence measurement, which hindered any determination of polarity patterns in this interval across the whole site (Clemens et al., 2016). Black and white zones: normal and reversed polarity, respectively; grey zones: magnetic polarity not clearly determined. All numbers are age assignations for boundaries and nannofossil events in Ma (Gradstein et al., 2012).

3.5 XRF scanning and calibration

U-channels were scanned at 1 cm intervals at The Australian National University (ANU) on a third-generation Avaatech XRF core scanner. All cores were scanned sequentially and standards measured daily were consistent across all runs. Core sections were covered with 4 µm thick Ultralene film and measured at 10 kv with a 500 µA current and no filter, then at 30 kv with a 200 µA current and Pd thin filter, and finally at 50 kv with a 50 µA current and Cu filter. A 30 s count time was used for all runs. Late Miocene XRF data generated at ANU (72.75 to 113.56 m CCSF) were spliced with data from Lübbers et al. (2019) (112.80 to 122.76 m CCSF), also scanned on an Avaatech XRF core scanner but with different machine settings. To splice the records, we rescaled the raw Lübbers et al. (2019) elemental count data so that absolute values and variance matched our data, based on an overlapping interval between 112.80 and 113.56 m CCSF.

Quantitative chemical compositions of a subset of discrete bulk sediment samples were determined at CEREGE after total digestion by inductively coupled plasma mass spectrometry (ICP-MS Agilent 7500ce). A total of 20 samples from the scanned late Miocene interval, selected to cover the range of values in the raw XRF count data for elements of interest, were analysed, and concentrations of Al, K, Ca, Ti, Mn, Fe, Rb, Sr, and Ba were determined. Prior to analysis, samples were dried and homogenized in a pestle and mortar. About 30 mg of sediment was completely dissolved by acid digestion using a 2 : 1 mixture of ultrapure acids (15 M HNO_3 and 22 M HF with $HClO_4$) on a hot plate. Blank contribution was estimated to be negligible. The accuracy of measurements was evaluated using analysis of geostandards MAG-1 (marine mud) and BE-N (basalt). The typical analytical uncertainty was better than 5 %. XRF-derived element counts were converted into element concentrations by direct linear calibration. This allowed us to reduce uncertainties related to the variable matrix effect and physical properties such as moisture content that typically change downcore. Linear calibration between element counts and concentrations in discrete samples over the interval ∼ 8.15 to 5 Ma showed significant coefficients of determination, with R^2 values ranging from 0.68 (Al) to 0.87 (Fe) (Fig. S3). For Ca and Sr, R^2 values were lower (0.39 and 0.42 respectively, Fig. S3) due to the consistently high Ca and Sr contents and small variability in the selected calibration samples. To estimate percent $CaCO_3$, we therefore used a Ca/Fe ratio calibration rather than a direct linear calibration. We first used the linear relationship between Ca/Fe counts and Ca/Fe as determined by ICP-MS (Fig. S3, $R^2 = 0.93$). Then $\%CaCO_3$ was calculated assuming that all Ca was contained in $CaCO_3$ – a reasonable assumption at Site U1443 given the relatively low clay content in lithological subunits Ib and IIa (Clemens et al., 2016). Additionally, we used calibrated XRF data to calculate biogenic

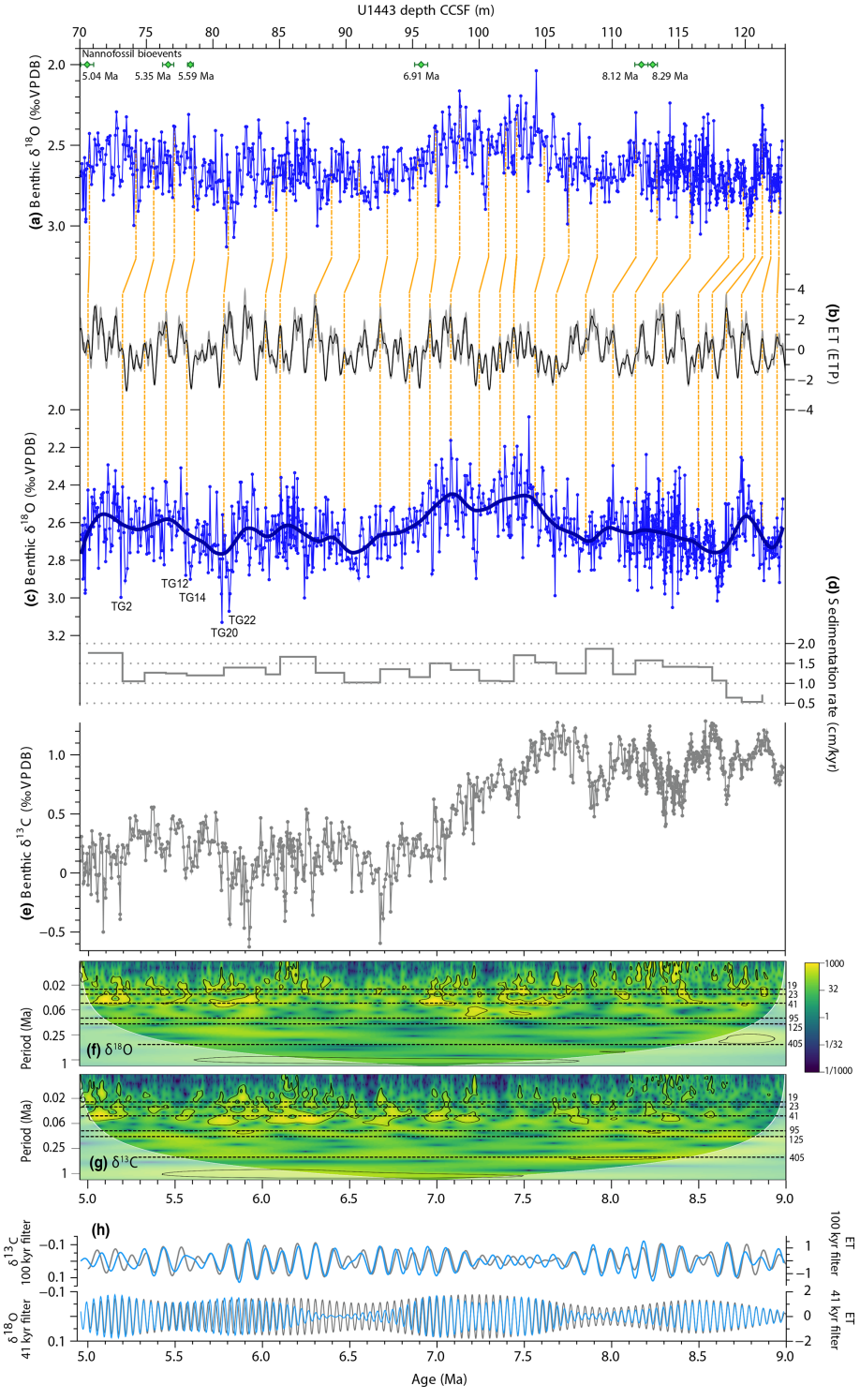

Figure 4. Astronomical (minimal) tuning of Site U1443 benthic δ^{18}O record to ET target. **(a)** Benthic δ^{18}O record on depth scale with nannofossil-based age constraints, **(b)** ET tuning target (1 : 1 weighting, normalized). ETP (1 : 0.5 : −0.4 weighting, normalized) is also shown in grey. Astronomical time series from Laskar et al. (2004). vc: tuned benthic δ^{18}O vs. age, **(d)** sedimentation rates, **(e)** tuned benthic δ^{13}C vs. age. Tie points between **(a)** and **(b)** are shown in orange (Table S3). An age–depth plot showing ET tie points and good agreement with biostratigraphic age control is shown in Fig. S1. **(f, g)** Wavelet analyses of tuned isotope records; white shaded area shows cone of influence, and contours show 95 % significance level. Main orbital periods are shown on the right in kyr. **(h)** Filtered tuned benthic isotope records compared to filtered ET (as in **b**). Top: 100 kyr filtered benthic δ^{13}C (blue; Gaussian filter centred on 100 kyr with bandwidth ±25 kyr to include 95 and 125 kyr peaks) compared with filtered ET (grey, identical filter design). Bottom: 41 kyr filtered benthic δ^{18}O (blue, Gaussian filter centred on 41.5 kyr with bandwidth ±1.5 kyr) compared with filtered ET (grey, identical filter design).

barium concentrations and "carbonate-free basis" (cfb) elemental concentrations, permitting evaluation of the extent to which dilution by the dominant sediment constituent (here $CaCO_3$) is driving trends and variability of more minor constituents in our records. To represent the relative contributions of $CaCO_3$ vs. terrigenous sediment components, we use the log count ratio of $Ca/(\sum(Al, K, Ti, Fe, Rb))$, termed log(Ca/Terr).

3.6 Ba-based export productivity proxies

The accumulation of biogenic barium in sediments is a reliable proxy for export production in certain environments (Paytan and Griffith, 2007). Micron-sized barite ($BaSO_4$) crystals are the main carriers of particulate barium in the ocean, with a maximum in concentration occurring just below the euphotic zone (Bishop, 1988; Dehairs et al., 1980). Although the exact mechanisms governing the precipitation of barite in the water column are only now coming to light (Martínez-Ruiz et al., 2019), its formation is thought to be associated with decaying organic matter. Depth profiles of dissolved Ba suggest that passive adsorption of barite onto mainly biogenic particles as they sink through the water column, combined with vertical mixing of dissolved Ba from the deep ocean and riverine input, can best explain Ba's nutrient-like water column distribution (Dehairs et al., 1980; Cao et al., 2016). Goldberg and Arrhenius (1958) first hypothesized that an increase in Ba accumulation rate in sediments underlying the equatorial Pacific divergence zone was directly linked to overlying high productivity, followed by similar observations in equatorial Indian Ocean sediments (Schmitz, 1987). Subsequently, evidence for strong correlations between fluxes of Ba and organic carbon in Atlantic and Pacific sediment traps led to algorithms relating new productivity to particulate Ba flux (Dymond et al., 1992; Francois et al., 1995). A further study focusing on the accumulation of barite (Ba_{barite}) extracted from core-top and late Pleistocene sediments refined its use as a proxy for export productivity (Paytan et al., 1996). Although significant Ba regeneration occurs in the uppermost few millimetres of sediment (Paytan and Kastner, 1996), barite dissolution is thought to cease after burial due to supersaturation in interstitial waters (Gingele and Dahmke, 1994; Dymond et al., 1992), and barite is not subject to burial diagenesis in oxic sediments (Paytan et al., 1993). Ocean sedimentary Ba has both a biogenic (Ba_{bio}) and a terrigenous ($Ba_{detrital}$) component, so estimates of past export productivity using barium must distinguish between these sources. This can either be done by chemical leaching of bulk sediment (assuming that all barite is Ba_{bio}) (e.g. Paytan et al., 1996), or by determination of total barium (Ba_{total}) and subtraction of $Ba_{detrital}$ using Al content and the terrigenous Ba/Al ratio, resulting in a record of Ba_{xs} ($Ba_{total} - Ba_{detrital}$); see Eq. (1) (Dymond et al., 1992).

$$[Ba_{xs}]_{ppm} = [Ba_{total}]_{ppm} - (Ba/Al_{terrigenous}) \cdot [Al_{total}]_{ppm} \quad (1)$$

Direct comparisons of measurements of Ba_{barite} and Ba_{xs} suggest that non-barite phases of barium may be included in the calculation of Ba_{xs}; nevertheless Ba_{xs} is most representative of Ba_{barite} and therefore export productivity in oxic carbonate-rich sediments with low terrigenous, biogenic silica, and organic carbon contents (Eagle et al., 2003; Averyt and Paytan, 2004; Gonneea and Paytan, 2006). The use of bulk Ba/Ti, Ba/Al, and Ba/Fe ratios is another approach to evaluate relative changes in export productivity (i.e. normalization to an element presumed to be predominantly of terrigenous origin), but without precisely predefining the Ba/terrigenous ratio that could vary over time, and also removing the effect of dilution by a dominant sedimentary component such as $CaCO_3$ (Murray et al., 2000).

Here, we reconstruct changes in export productivity at Site U1443 over the late Miocene using XRF-derived Ba data and compare elemental count ratios of log(Ba/Fe), log(Ba/Ti), and log(Ba/Al), with $[Ba]_{cfb}$ and $[Ba]_{xs}$ calculated following Eq. (1), using a $Ba/Al_{terrigenous}$ value of $0.0075\ g\ g^{-1}$ following Dymond et al. (1992). To verify consistency of trends, we also calculate $[Ba]_{xs}$ using [Ti] to represent $Ba_{detrital}$, applying a $Ba/Ti_{terrigenous}$ ratio of $0.183\ g\ g^{-1}$ (McLennan, 2001), and carbonate-free $[Ba]_{xs}$.

3.7 Mass accumulation rates

MARs of bulk sediment, $CaCO_3$, $[Ba]_{xs}$, and summed terrigenous elements (Al, K, Ti, Fe, and Rb) were calculated by multiplying concentrations by linear sedimentation rates (in $cm\ kyr^{-1}$) derived from our new age model and dry bulk densities (in $g\ cm^{-3}$). Dry bulk density values were estimated from high-resolution shipboard gamma ray attenuation bulk density scanning data and the linear relationship between all shipboard U1443 wet bulk density and dry bulk density measurements ($n = 164$, $R^2 > 0.99$) (Clemens et al., 2016). Units are $g\ cm^{-2}\ kyr^{-1}$ for bulk and $CaCO_3$ MAR, $\mu g\ cm^{-2}\ kyr$ for $[Ba]_{xs}$ MAR and $mg\ cm^{-2}\ kyr^{-1}$ for terrigenous MAR.

3.8 Time series analysis

Spectral analyses of benthic isotope and XRF data against tuned age were performed on detrended records (bandpass filtered to remove signals with periods longer than one-third of the length of each dataset) with a constant time step of 0.5 kyr for XRF records and 2 kyr for isotope records. Multitaper method (MTM) spectral analyses using a robust red-noise model were performed using Acycle (Li et al., 2019). Blackman–Tukey cross-spectral analyses were performed in Arand to assess phase and coherence (Howell et al., 2006). Wavelet analyses were performed in R using the biwavelet package (Gouhier et al., 2018; Grinsted et al., 2004). To illustrate precession-band variance and amplitude modulation, certain records (with identified significant precession variance) were filtered using a Tanner–Hilbert filter centred on

46.5 cycles Myr^{-1} with bandwidth ±8.5 (designed to include all precession terms with periods between 18 and 26 kyr) in Acycle (Li et al., 2019).

4 Results

4.1 Age model and benthic foraminiferal isotope data

U1443 benthic δ^{18}O and δ^{13}C data between 70.06 and 122.76 m CCSF are shown in the depth domain in Fig. 3 alongside calcareous nannofossil datums (revised herein, Table S2) and magnetochron boundaries. Our tuned benthic δ^{18}O and δ^{13}C records, shown in Fig. 4, span the interval 8.99 to 4.96 Ma, and our age model shows excellent agreement with revised biostratigraphic and shipboard magnetostratigraphic datums (Fig. S1). Sedimentation rates generally vary between 1 and 1.7 cm kyr^{-1}, with a minimum of ∼ 0.5–0.7 cm kyr^{-1} in the oldest part of the record (9 to 8.6 Ma) and a maximum of ∼ 1.9 cm kyr^{-1} at 8 to 7.8 Ma (Fig. 4d). Between 112.86 and 121 m CCSF (8.7–8.1 Ma), our age model differs by up to 60 kyr from that of Lübbers et al. (2019), which is based on correlation of Site U1443 benthic δ^{18}O and δ^{13}C data to the orbitally tuned ODP Site 1146 δ^{13}C record (Holbourn et al., 2018) using a limited number of tie points (Site locations in Fig. 1c). Both wavelet analyses (Fig. 4f, g) and spectral analyses (Fig. S2e, f) of the tuned benthic records reveal significant (> 99 %) orbital periodicities of ∼ 405 and 41 kyr for δ^{18}O and ∼ 405, 125, 95, 53, and 41 kyr for δ^{13}C, and filtered isotope records show good correspondence with filtered ET (Fig. 4h). Cross-spectral analysis between δ^{18}O and δ^{13}C reveals > 95 % coherency in the 41 and 405 kyr bands (Fig. S4a). Our age model is supported by close agreement between Site U1443 benthic δ^{18}O and δ^{13}C data and independent orbitally tuned benthic isotope records from the South China Sea (ODP 1146) (Holbourn et al., 2018, 2021), equatorial Pacific (IODP Sites U1338 and 1337) (Drury et al., 2016, 2018, 2017), and equatorial Atlantic (ODP Sites 926 and 999) (Bickert et al., 2004; Shackleton and Hall, 1997; Drury et al., 2017; Zeeden et al., 2013) (Figs. S5, S6).

Mean temporal resolution of the Site U1443 benthic isotope record is 4.2 kyr. Between 9 and 7.6 Ma, mean benthic δ^{18}O values vary between 2.5 ‰ and 2.8 ‰, with an overall decreasing trend culminating in minimum values averaging ∼ 2.4 ‰ between 7.6 and 7 Ma (Fig. 4c). Between 7 and 6.5 Ma, mean δ^{18}O values increase by ∼ 0.25 ‰, and between 6.5 and 5 Ma, mean values vary between 2.55 ‰ and 2.8 ‰. Between 6 and 5 Ma, a number of prominent benthic δ^{18}O maxima are identified in the U1443 δ^{18}O record, namely TG2, TG12, TG14, TG20, and TG22 (following nomenclature of Shackleton et al., 1995) (Fig. 4c). Between 7.7 and 6.9 Ma, strong obliquity modulation of the U1443 δ^{18}O record is seen (Fig. 4f), as also noted at Sites U1337 (Drury et al., 2017) and 1146 (Holbourn et al., 2018) (Fig. S5). Long-term trends are similar to those recorded

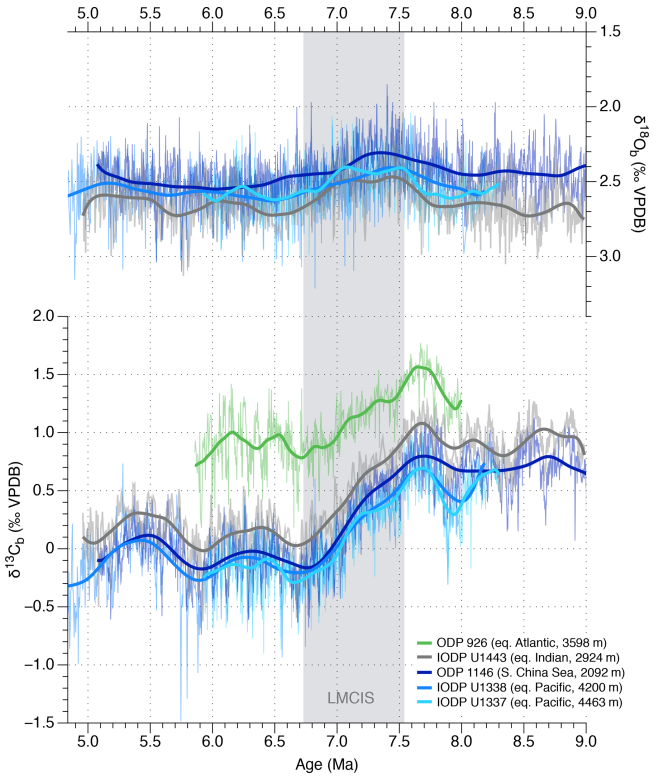

Figure 5. Late Miocene evolution of low-latitude deep-ocean interbasin benthic δ^{13}C and δ^{18}O gradients. South China Sea ODP Site 1146 (Holbourn et al., 2018) with age model revised in Holbourn et al. (2021), equatorial Pacific IODP Sites U1338 (Drury et al., 2018, 2016) and U1337 (Drury et al., 2017), and ODP Site 926 (Shackleton and Hall, 1997; Drury et al., 2017; Zeeden et al., 2013). All records are shown on their latest independent orbitally tuned chronologies. We have excluded Caribbean ODP Site 999 from this figure because it is bathed in intermediate water masses due to basin geometry and sill depths (Bickert et al., 2004). Deep South Atlantic Site 704 (Müller et al., 1991) data are not plotted due to clear age model discrepancies when compared to orbitally tuned records. All δ^{18}O records are based on *Cibicidoides wuellerstorfi* or *C. mundulus*; therefore no corrections are applied, following Jöhnck et al. (2021). The Site 926 record includes δ^{13}C corrections for some samples due to the multispecific nature of the record (Drury et al., 2017). No correction was applied to *C. wuellerstorfi* or *C. mundulus* δ^{13}C values.

at Pacific sites, with benthic δ^{18}O values at Indian Ocean Site U1443 ∼ 0.1 ‰ heavier than at Pacific Sites U1337 and U1338 and ∼ 0.2 ‰–0.3 ‰ heavier than at South China Sea Site 1146 (Fig. 5a).

Mean benthic δ^{13}C values at Site U1443 vary between 0.7 ‰ and 1.1 ‰ from 9 to 7.6 Ma, then decrease from ∼ 1 ‰ to −0.2 ‰ between 7.6 and 6.7 Ma, reflecting the globally recognized Late Miocene Carbon Isotope Shift (LMCIS) (Keigwin, 1979; Keigwin and Shackleton, 1980) (Fig. 4e). From 6.7 to 5 Ma, mean values vary between −0.2 ‰ and 0.4 ‰. The timing of the LMCIS at Site U1443 (∼ 7.6 to

~ 6.7 Ma) is synchronous with the event in independent orbitally tuned high-resolution records (Drury et al., 2018, 2017; Holbourn et al., 2018; Drury et al., 2016) (Figs. 5b, S6), and its magnitude (~ 1 ‰ decrease in $\delta^{13}C$ in smoothed record) is similar to that recorded in Pacific Ocean sediments from Sites U1338, U1337, and 1146. The Site U1443 $\delta^{13}C$ record shows a consistent positive offset of 0.15 ‰–0.25 ‰ relative to South China Sea Site 1146 over the 9 to 5 Ma interval (Fig. 5b).

4.2 XRF data

Scanning XRF results are shown in Fig. 6. Raw and calibrated elemental data show consistent trends and amplitude variability (Fig. 6). For Ti, Ba, Al, and Mn, the re-scaled counts-per-second values in the 113.37 to 122.76 m CCSF interval (Lübbers et al., 2019) fell outside of our calibration range; thus data below 113.6 m (~ 8.15 Ma) were not converted to concentrations (Fig. 6). In brief, Al, Si, Ti, Fe, Rb, and K show similar trends, with a long-term small increase in concentrations from 8.15 to 5 Ma and spikes (particularly pronounced in Rb and K) corresponding in some cases to described ash layers (Clemens et al., 2016). Ca and Ba show a minor long-term decrease over the study interval, while Sr and Mn increase from ~ 8.15 to 6 Ma and then stabilize or decrease slightly. All elements show high-frequency variability throughout. Confidence in our method of calculating $CaCO_3$ content is provided by very good agreement with independent $\%CaCO_3$ estimates for the middle and early late Miocene interval of Site U1443 based on calibration of XRF-derived counts of $(Ca/\sum(Ca, Al, Si, K, Ti, Mn, Fe, S))$ to discrete $CaCO_3$ measurements (Lübbers et al., 2019), including an overlapping interval based on an alternate splice from 112.8 and 113.6 m CCSF (Fig. 7b).

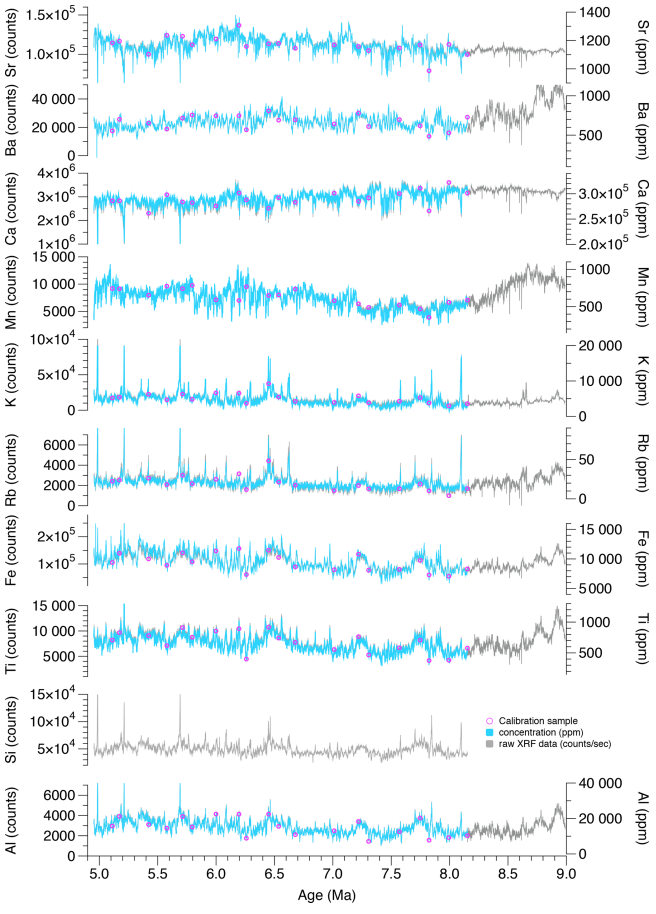

Figure 6. Raw counts per second (grey lines) and calibrated concentration (blue lines) scanning XRF elemental data over the late Miocene interval. Pink circles show samples used for calibration (see Fig. S3).

4.3 $CaCO_3$ content, sediment accumulation patterns, and Ba proxies

Late Miocene estimated $\%CaCO_3$ varies between ~ 60 % and 90 % with a slight long-term decrease over the 9 to 5 Ma interval (Fig. 7b). This long-term trend is also visible in the log(Ca/Terr) record (Fig. 7c), implying a small increase in the contribution of terrigenous material relative to $CaCO_3$ in Site U1443 sediments over time. Three $\%CaCO_3$ and log(Ca/Terr) minima between 6 and 5 Ma occur in identified ash layers. Log(Ba/Al), log(Ba/Fe), and log(Ba/Ti) show identical long-term and orbital-scale trends (Fig. S7); therefore we only discuss log(Ba/Fe) in the main text. Log(Ba/Fe) shows a long-term decrease between 9 and 5.3 Ma, and a smaller increase from 5.3 to 5 Ma (Fig. 7d). $[Ba]_{xs}$ shows identical variability whether calculated using Al or Ti (Fig. 7e) and generally shows similar patterns to log(Ba/Fe) where records overlap (8.15 to 5 Ma). Values of $[Ba]_{xs}$ generally vary between 400 and 800 ppm (representing on average 83 % of total [Ba]), and carbonate-free $[Ba]_{xs}$ concentrations are typically 1000 to 4000 ppm (Fig. S7). A peak in log(Ba/Fe) between 7.6 and 7.3 Ma is less pronounced in the $[Ba]_{xs}$ record but is prominent in the carbonate-free $[Ba]_{xs}$ record (Fig. S7, grey shading), suggesting that this peak is suppressed in the $[Ba]_{xs}$ record as a result of dilution by carbonate. The trough between 7.9 and 7.6 Ma seen in log(Ba/Fe) and $[Ba]_{xs}$ and to a lesser extent in $\%CaCO_3$, log(Ca/Terr), and carbonate-free $[Ba]_{xs}$ appears not to be an artefact of dilution.

Bulk sediment MARs vary between 0.5 and 2.1 $g\,cm^{-2}\,kyr^{-1}$ with a step increase from ~ 0.5 to 1.5 $g\,cm^{-2}\,kyr^{-1}$ occurring at 8.66 Ma (Fig. 7g), concurrent with a major sedimentation rate increase (Fig. 4d). The stepwise nature of MAR records results from age-model-imposed stepped changes in sedimentation rate. $CaCO_3$ MARs range from 0.4 to 2 $g\,cm^{-2}\,kyr^{-1}$ and co-vary with bulk sediment MARs, with the increasing difference between the two records reflecting a small long-term increase in non-$CaCO_3$ components (Fig. 7g). This small increase is reflected in terrigenous element MARs, which vary between

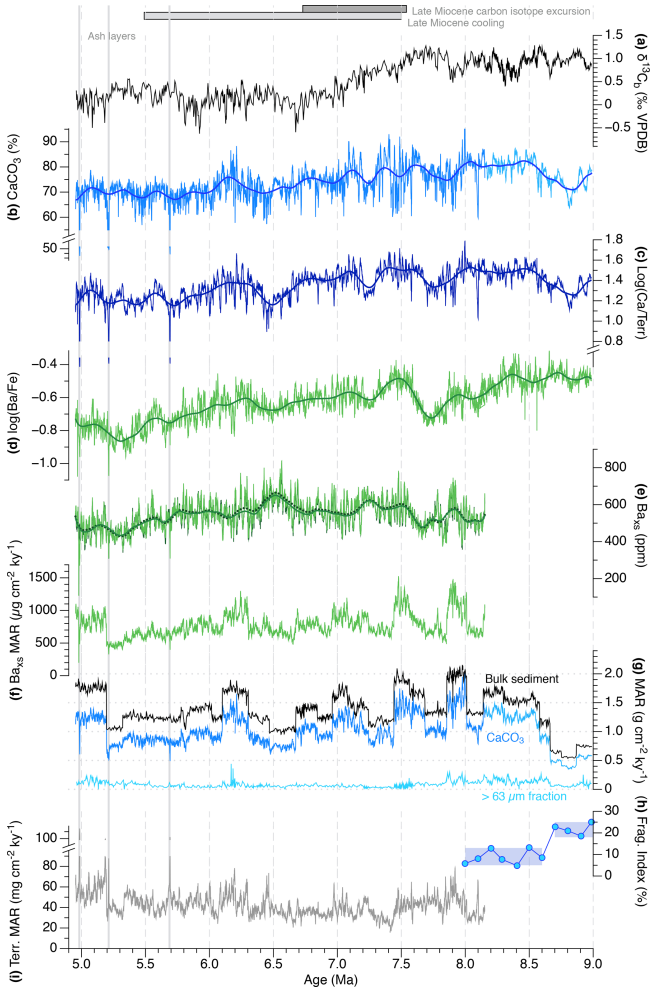

Figure 7. XRF-derived late Miocene $CaCO_3$ and export productivity records from Site U1443. **(a)** Benthic $\delta^{13}C$; **(b)** percent $CaCO_3$; **(c)** log(Ca/Terr); **(d)** log(Ba/Fe); **(e)** Ba_{xs} calculated with both [Al] (light green) and [Ti] (dark green); **(f)** $[Ba]_{xs}$ MAR; **(g)** bulk (black), $CaCO_3$ (blue), and > 63 µm fraction (light blue) MAR; **(h)** foraminiferal fragmentation index (Le and Shackleton, 1992); **(i)** terrigenous (Al + Fe + Ti + K + Rb) MAR. For $CaCO_3$ records, lighter blue lines are based on % $CaCO_3$ from Lübbers et al. (2019) and darker blue lines are based on % $CaCO_3$ estimates in this study. The late Miocene carbon isotope excursion and the main interval of late Miocene SST cooling are shown as grey bars. Shaded intervals are identified ash layers.

~ 20 and 80 mg cm^{-2} kyr^{-1} (excluding volcanic ash layers) (Fig. 7i). We note that absolute values of terrigenous MAR should be interpreted with caution, because this calculation does not include Si as this element was not quantified in discrete samples. Nevertheless, a significant correlation between Al and Si counts ($R^2 = 0.8$, Fig. 6) suggests that Si is primarily of terrigenous origin; therefore trends in log(Ca/Terr) and terrigenous MAR in Fig. 7 are likely robust despite the exclusion of Si. From 8.3 to 5 Ma, $[Ba]_{xs}$ MAR shows similar patterns to $CaCO_3$ MAR, with no clear long-term trend and maximum values driven by higher sedimentation rates in the intervals 5.2 to 5, 6.3 to 6.1, 7.7 to 7.5, and 8 to 7.8 Ma (Fig. 7f).

Spectral analyses reveal significant orbital periods in all late Miocene XRF records (Fig. 8). The ~ 405 kyr period is > 99 % significant in [Al], [Ba], $[Ba]_{cfb}$, $[Ba]_{xs}$, and log(Ba/Fe), whereas the ~ 125 kyr period is significant (> 95 % or > 99 %) in [Ba], $[Ba]_{cfb}$, $[Ba]_{xs}$, log(Ba/Fe), and %$CaCO_3$ records. At higher frequencies, the spectral signatures of [Fe], [Al], [Ti], and [Ba] are dominated by significant peaks at 24 kyr (> 99 %) and 41 kyr (> 90 %), with [Ba] additionally showing peaks at 22.5 kyr (> 99 %) and at 26 and 30 kyr (> 95 %). Log(Ba/Fe), $[Ba]_{cfb}$, and $[Ba]_{xs}$ show dominant (> 99 % significant) 22.5 kyr variability, with additional > 95 % significant peaks at 24 and 30 kyr (for $[Ba]_{xs}$ only). Log(Ca/Terr) shows significant peaks at 24 and 22.5 kyr (both > 99 %), and also at 68 kyr (> 95 %). Percent $CaCO_3$ contains significant (> 95 %) variability at 22.5 kyr, with additional peaks at 68 and 37 kyr. In summary, all records show highly significant variability in the precession band (22–24 kyr), with variability at the 22.5 kyr period and the ~ 125 kyr period most strongly associated with the biogenic component of Ba and with $CaCO_3$. Wavelet analyses of log(Ba/Fe) and $[Ba]_{xs}$ confirm significant precession-scale variability in these records throughout the 9 to 5 Ma interval (Fig. 9).

5 Discussion

5.1 Late Miocene sedimentation patterns in the southern Bay of Bengal

We first examine the drivers of changes in sediment MAR identified in our record, and their possible link to regional and global productivity trends. The 3-fold increase in $CaCO_3$ MAR at 8.66 Ma at Site U1443, originally described in Lübbers et al. (2019), could result from improved preservation and/or increased carbonate export by pelagic calcifiers (coccolithophores and/or foraminifera). Based on $CaCO_3$ percentages, MARs, and benthic to planktic foraminiferal ratios, Lübbers et al. (2019) identified the middle to late Miocene "carbonate crash" in Site U1443 sediments between ~ 12.2 and 10 Ma, with a slow recovery from ~ 10 to 8.7 Ma, favouring an interpretation that the increase in $CaCO_3$ MAR at 8.66 Ma reflects improved preservation. A record of planktic foraminiferal fragmentation between 9 and 8 Ma generated in the present study, interpreted to reflect a decrease in carbonate dissolution (Le and Shackleton, 1992), supports this interpretation (Fig. 7h). We see no change in log(Ba/Fe) concurrent with the $CaCO_3$ MAR increase at 8.66 Ma, which suggests that total export productivity at Site U1443 remained stable over this transition. However, our data suggest that an increase in coccolithophore production may have occurred. The contribution of foraminifera to total $CaCO_3$ over our study interval is low (see > 63 µm MAR in Fig. 7g),

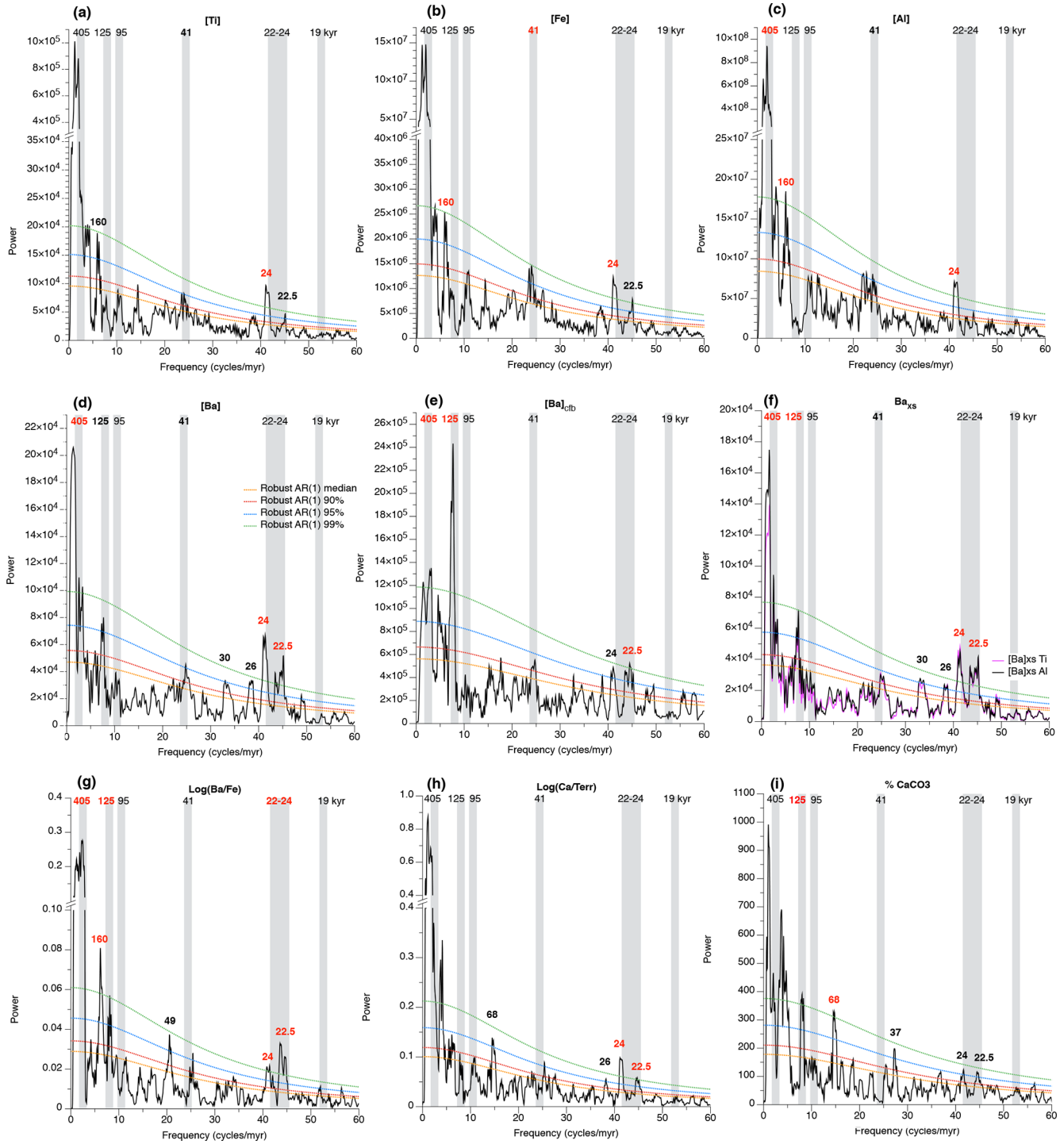

Figure 8. Spectral analyses for over the 9 to 5 Ma interval (log ratios and % $CaCO_3$) or 8.15 to 5 Ma interval (calibrated element concentrations and $[Ba]_{xs}$). **(a)** [Ti], **(b)** [Fe], **(c)** [Al], **(d)** [Ba], **(e)** $[Ba]_{cfb}$ (carbonate free basis), **(f)** $[Ba]_{xs}$, **(g)** log(Ba/Fe), **(h)** log(Ca/Terr), **(i)** % $CaCO_3$. Grey bands denote primary orbital periods based on the La04 astronomical solution. The 22–24 kyr band covers two peaks centred at 23.5 and 22.3 kyr.

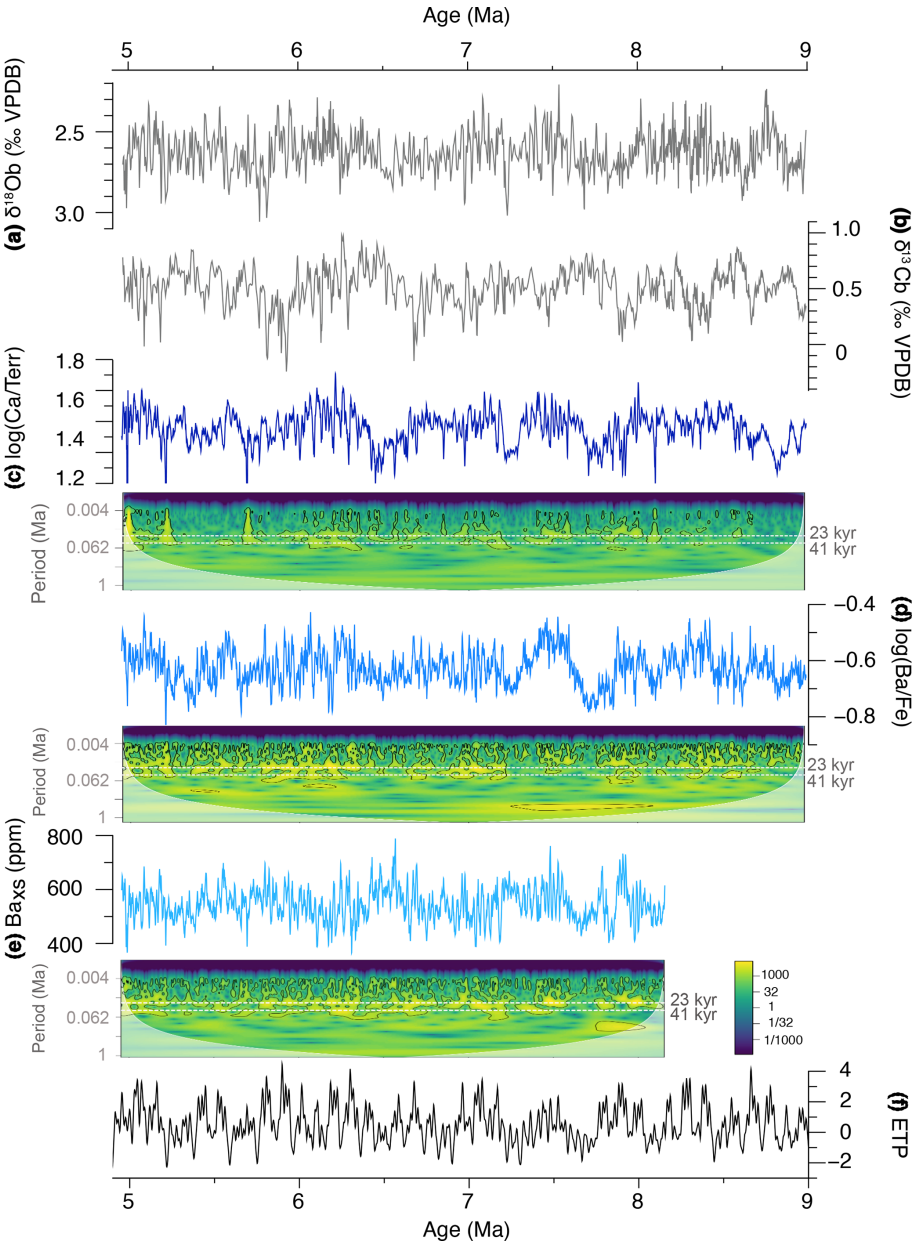

Figure 9. Orbital-scale variability of productivity and $CaCO_3$ proxies at Site U1443. All records shown here are bandpassed as described in the methods. **(a)** Benthic $\delta^{18}O$, **(b)** benthic $\delta^{13}C$, **(c)** log(Ca/Terr), **(d)** log(Ba/Fe), **(e)** $[Ba]_{xs}$, **(f)** ETP. For panels **(c)**–**(e)**, wavelet analyses are shown, illustrating dominant precession-scale (22–24 kyr) variability in Ba proxies and both precession and obliquity (41 kyr) variability in log(Ca/Terr).

leading us to infer that higher $CaCO_3$ MARs between 8.66 and 5 Ma are primarily driven by coccoliths. A 3-fold increase in sediment accumulation rate at ∼ 8.6 Ma with no change in $CaCO_3$ content (%), implying a large increase in $CaCO_3$ MARs, is also seen at shallower (2247 m) Deep Sea Drilling Project (DSDP) Site 216 on the NER near the Equator (Fig. 1c) (Bukry, 1974; McNeill et al., 2017; Pimm, 1974). This suggests that production played a role in driving regional carbonate MAR increases as well as improved preservation at deeper sites. A recent study decoupling coccolith and foraminiferal MARs in relatively shallow, globally distributed sites (minimally affected by dissolution) records a late Miocene pulse in coccolith MARs beginning at ∼ 9 to 8 Ma and persisting into the Pliocene at ∼ 4 to 3 Ma, which is interpreted to reflect high coccolithophore productivity and calcification driven by weathering alkalinity inputs and regional nutrient changes (Si and Rosenthal, 2019).

Interestingly, the increase in bulk MARs at 8.66 Ma is driven by both $CaCO_3$ and to a lesser extent non-$CaCO_3$ components (clays), implicating another mechanism as well as improved carbonate preservation and increased coccolith export productivity affecting sedimentation at Site U1443. Miocene Site U1443 clays are thought to be primarily supplied by the major rivers, with limited contribution of fine-grained mineral dust originating from the deserts bordering the Arabian Sea (Bretschneider et al., 2021), suggesting that an increase in dust delivery at this time is an unlikely candidate for driving the $\sim 50\,\%$ increase in clay content. We speculate that an increase in coccolith $CaCO_3$ flux to the seafloor could have led to increased scavenging by sinking biogenic aggregates of fine clays. Fine clays are present in the southern BOB water column as a direct result of riverine flux (Rixen et al., 2019; Ramaswamy, 1993), and in nepheloid layers above the NER where high clay concentrations occur due to proximity to the sedimentary fan systems to the east (Nicobar Fan) and west (Bengal Fan) (Stow et al., 1990). Recent studies of sedimentation patterns on the Bengal and Nicobar Fans, separated by the NER, interpret a large increase in sediment accumulation rate both on the NER and the Nicobar Fan at $\sim$ 10 to 8 Ma to reflect increased lithogenic sediment flux to the eastern Indian Ocean (McNeill et al., 2017; Pickering et al., 2020b). Our data from the NER show that $> 75\,\%$ of the 3-fold increase in sediment accumulation rate at 8.66 Ma is driven by biogenic $CaCO_3$; thus we caution against using sediment accumulation rate at Site U1443/758 as representative of changes in sediment flux to the Bengal–Nicobar Fan system. Data from Site U1443, as well as from nearby DSDP Site 216 (Bukry, 1974; McNeill et al., 2017; Pimm, 1974) (Fig. 1c), suggest that increases in biogenic carbonate accumulation on the NER are decoupled, both temporally and mechanistically, from the increase in sediment delivery to the Nicobar Fan system. The gradual increase in terrigenous element and non-$CaCO_3$ MARs over the 9 to 5 Ma interval seen at Site U1443 (Fig. 7g, i) is part of a longer-term trend of increasing mineral flux in this region of the NER from the Miocene to the Pleistocene, beginning at $\sim$ 12 Ma at ODP Site 758, that is thought to reflect increased Himalayan erosion (Ali et al., 2021; Hovan and Rea, 1992).

Increases in the MAR of biogenic components ($CaCO_3$, opal, organic carbon, phosphorus) between $\sim$ 9 and 4 Ma have been measured in sediments from the Pacific, Indian, and Atlantic Oceans (Farrell et al., 1995; Lyle and Baldauf, 2015; Van Andel et al., 1975; Grant and Dickens, 2002; Delaney and Filippelli, 1994; Hermoyian and Owen, 2001; Dickens and Owen, 1999; Drury et al., 2021). This period of increased biogenic sedimentation, supported by independent paleoproductivity proxies (e.g.Diester-Haass et al., 2005), is thought to reflect higher biological productivity and was dubbed the "biogenic bloom" by Farrell et al. (1995). A low-resolution $CaCO_3$ MAR record from Site 758 shows higher values between 8 and 4 Ma, which in the absence of evidence for an increase in carbonate dissolution at 4 Ma could suggest an end to the biogenic bloom at this site in the early Pliocene (Dickens and Owen, 1999; Pierce et al., 1989; Si and Rosenthal, 2019), although improved age control for the Pliocene interval and independent paleoproductivity reconstructions are needed to verify this. Hypotheses to explain the biogenic bloom invoke a change in global nutrient cycling; i.e. a global increase in nutrient input, and/or redistribution of nutrients between basins (Grant and Dickens, 2002), although the asynchronous timing of the biogenic bloom between regions, its variable expression, and its differentiation from the carbonate crash recovery complicate its interpretation. Diester-Haass et al. (2006) hypothesized that changes in reconstructed productivity were correlated to the LMCIS at four Indo-Pacific sites and tentatively proposed a link to a strengthened wind regime at this time. At Site U1443, we find no clear link between export productivity or carbonate sedimentation and the LMCIS (Fig. 7). In the northern Indian Ocean, the influence of possible concurrent changes in monsoon strength on paleoproductivity and biogenic MARs must also be considered, and these are discussed in Sect. 5.3.

5.2 Orbital forcing of late Miocene South Asian summer monsoon winds

On orbital timescales, time series analyses reveal dominant precession-band (22–24 kyr) variance in late Miocene export productivity records (Figs. 8, 9). Spectral analyses of individual calibrated time series of [Ba], [Al], [Fe], [Ti], $[Ba]_{cfb}$, and $\%CaCO_3$ allow us to tease apart the effects of sediment dilution and the competing influence of Ba_{terr} and Ba_{bio} on our Ba proxies, $[Ba]_{xs}$ and log(Ba/Fe). The 41 kyr obliquity period is most significant ($> 90\,\%$) in the terrigenous element records (Al, Fe, Ti, Ba), and absent or less significant in $[Ba]_{xs}$, log(Ba/Fe), log(Ca/Terr), and $\%CaCO_3$ (Fig. 8). The 24 kyr period stands out as highly significant in all records ($> 99\,\%$, except for $\%CaCO_3$ and $[Ba]_{cfb}$ where $> 95\,\%$). In contrast, the 125 and 22.5 kyr peaks that dominate the $[Ba]_{xs}$ and log(Ba/Fe) spectra ($> 99\,\%$ significant) are also highly significant only in the [Ba], $[Ba]_{cfb}$, $\%CaCO_3$, and log(Ca/Terr) records. This suggests that strong variability at the 125 kyr (eccentricity) and 22.5 kyr (precession) periods is related to biological productivity (i.e. Ba_{bio} and not $Ba_{detrital}$, as well as biogenic $CaCO_3$). The 30 kyr peak in $[Ba]_{xs}$ is also seen in [Ba] but not in [Fe], [Al], or [Ti], so we similarly interpret this period as being related to biological productivity. The 23.6 and 22.3 kyr periods (highlighted together in Fig. 8 as one grey band spanning 22–24 kyr) are primary periods of Earth's precession, whereas the 53 and 41 kyr periods are related to Earth's obliquity (Laskar et al., 2004).

Although our export productivity records are of sufficient resolution to detect it, half-precession ($\sim$ 11 kyr) cycles were not identified in spectral analyses. The presence of half-precession cycles might be expected because the bi-annual primary productivity peak observed today in southern BOB waters (Fig. 2) could fuel high productivity during both pre-

cession minima (strong summer winds) and precession maxima (strong winter winds). The lack of a half-precession signal could be explained by the distinct particle export seasonality, such that the fraction of net primary productivity exported from the photic zone and accumulating in underlying sediments is strongly biased towards the late summer months (Fig. 2d, e), perhaps as a result of increased ballasting by terrigenous particles carried into the BOB by summer monsoon runoff. Thus, the winter productivity maximum appears not to be efficiently transferred to the fossil record.

Significant variability at obliquity and precession periods has been identified in high-resolution late Miocene–early Pliocene records of precipitation–runoff based on planktic foraminiferal $\delta^{18}O$ and seawater $\delta^{18}O$ in the nearby Andaman Sea (Jöhnck et al., 2020). These authors suggest that, prior to a distinct switch to obliquity-driven variability around 5.55 Ma, their records reflect strong precession (insolation) control on South Asian monsoon rainfall from 6.2–5.55 Ma, with significant phase lags between proxy variations and precession. Wavelet analyses of log(Ba/Fe) and $[Ba]_{xs}$ show that precession-band (22–24 kyr) variability dominated throughout our 9 to 5 Ma study interval at Site U1443 (Fig. 9). Although phase relationships with insolation should be interpreted with caution because of errors inherent in our late Miocene age model, export productivity appears to be coherent and in phase (within error) with the Summer Inter-Tropical Insolation Gradient, SITIG (the insolation gradient between 23° N and 23° S on 21 June) (Fig. S4d). SITIG has been proposed as a primary control on the strength of SASM winds, because a stronger SITIG increases the pressure gradient between the two limbs of the winter hemisphere Hadley cell, which drives monsoon winds into the summer hemisphere (Bosmans et al., 2015). Our new Ba-based export productivity records corroborate the hypothesis that insolation played a dominant role in driving late Miocene South Asian summer monsoon wind variability in the equatorial sector of the SAM region, as predicted by general circulation models (Bosmans et al., 2018). We infer that internal climate processes such as ice volume played a more minor role than in the Late Pleistocene, when large glacial–interglacial cycles and related feedbacks drove variability in the Asian monsoon on 100 kyr timescales (Clemens et al., 2018, 2021), and SASM wind proxies from the Arabian Sea and southern BOB record up to $\sim$ 9 kyr phase lags relative to precession (Bolton et al., 2013; Caley et al., 2011; Clemens and Prell, 2003; Clemens et al., 1991). A half-precession cycle related to equatorial insolation has been previously identified in Miocene and Pleistocene climate proxy records (Fox et al., 2017; Bolton et al., 2013; Sun and Huang, 2006). The lack of a half-precession signal in our records corroborates the idea that the SITIG, rather than local insolation (which contains a significant half-precession component between the Equator and 5° latitude), was the primary driver of export productivity variations at our site.

In addition to the periods discussed above, a number of non-primary orbital periods termed heterodynes, which result from non-linear interactions between variables operating at Earth's primary orbital periods (Rial and Anaclerio, 2000; Thomas et al., 2016; Clemens et al., 2010), stand out in our late Miocene records (24, 26, 30, 37, 49, and 68 kyr periods; Fig. 8). For example, the 1/24 kyr heterodyne, prominent in all our records, could result from the interference between eccentricity and precession, and the 1/30 kyr heterodyne seen in Ba records from an interaction between obliquity and precession. Several of these heterodynes have been previously identified in spectra of seawater $\delta^{18}O$ that reflect Asian monsoon precipitation and runoff, both in the Andaman Sea (30 and 130 kyr during the Pleistocene, 27 and 30 kyr in the latest Miocene) (Gebregiorgis et al., 2018; Jöhnck et al., 2020) and in the East China Sea (29 and 69 kyr during the Pleistocene) (Clemens et al., 2018), suggesting high sensitivity of the monsoon to orbital forcing. We favour the interpretation that the prominent 24 kyr variability in our records reflects a primary period of precession, because precession filters of $[Ba]_{xs}$ and log(Ba/Fe) spanning 18 to 26 kyr show strong amplitude modulation of the precession signal at a period of $\sim$ 405 kyr, which results from the interaction of the 23.6 and 22.3 kyr periods $(1/[(1/22.3) - (1/23.6)] = 404.8$ kyr) (Fig. 10). Amplitude modulation of precession-scale variability in our productivity records broadly follows that of SITIG (Fig. 10), suggesting a direct response of SASM winds to cross-equatorial insolation gradients during the late Miocene.

Cross-spectral analysis of our $[Ba]_{xs}$ productivity record with the Site U1448 seawater $\delta^{18}O$ record (Jöhnck et al., 2020) over the interval 6.19 to 4.95 Ma (where records overlap) shows > 80 % coherency and an in-phase relationship at the 30 kyr period, suggesting that monsoon winds and precipitation–runoff in the BOB were to some degree coupled on orbital timescales during this time (Fig. S4c), as is the case in the late Pleistocene (Clemens et al., 2021). Nevertheless, our $[Ba]_{xs}$ record over this interval contains stronger primary precession (22–24 kyr) and obliquity (41 kyr) signals than the Site U1448 seawater $\delta^{18}O$ record, which cannot be explained by differences in resolution, highlighting that different climatic processes and feedbacks operating on orbital timescales must contribute to the two records (interpreted to reflect runoff/precipitation and wind, respectively) to different extents. In the late Pleistocene, strong obliquity-band and precession-band variance is found in Andaman Sea proxy records of monsoon precipitation–runoff (Gebregiorgis et al., 2018), whereas records of upper ocean stratification controlled by South Asian monsoon wind mixing at Site 758 ($\sim$ 100 m from Site U1443) show only precession-band variance (Bolton et al., 2013). The significant 41 kyr variability seen in late Miocene terrigenous elements at Site U1443 (Fig. 8a–c) could also suggest obliquity control on monsoon runoff into the BOB at this time. Clemens et al. (2021) show that 100 and 41 kyr variability are at least as important as preces-

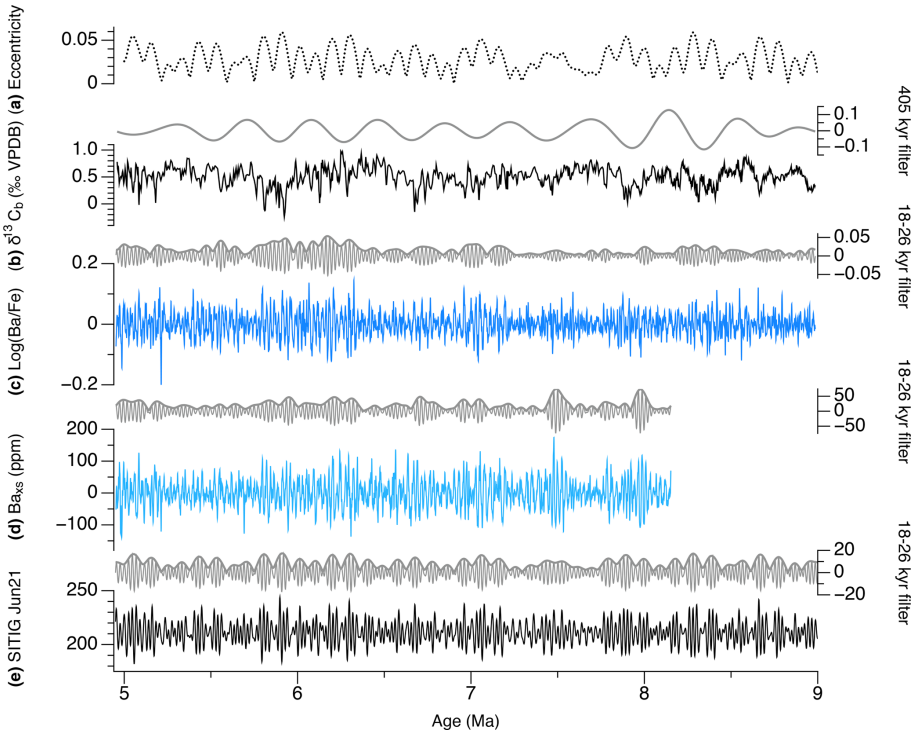

Figure 10. Detrended and filtered late Miocene U1443 records to illustrate precession-band variance and amplitude modulation. **(a)** Eccentricity (Laskar et al., 2004), **(b)** benthic δ^{13}C (bandpassed as in Fig. 9), and its 405 kyr filter (above) (note reversed y axes). **(c)** Lowess-detrended log(Ba/Fe) (window = 0.1 Ma) and 18 to 26 kyr filter (above), **(d)** Lowess-detrended Ba_{xs} (window = 0.1 Ma) and its 18 to 26 kyr filter (above), **(e)** the summer inter-tropical insolation gradient (SITIG, calculated as the insolation difference between 23° N and 23° S on 21 June using orbital solution of Laskar et al., 2004), and its 18 to 26 kyr filter and amplitude modulation (above); for panels **(c)**–**(e)**, raw datasets were filtered using a Tanner–Hilbert filter centred on 46.5 cycles Myr^{-1} with bandwidth ±8 (designed to include all precession terms with periods between 18 and 26 kyr). For panel **(b)**, a Tanner–Hilbert filter centred on 2.47 cycles Myr^{-1} with bandwidth ±0.8 was applied.

sion in Pleistocene proxy records of monsoon precipitation–runoff in the Bay of Bengal and suggest that summer monsoon precipitation is strongly influenced by global boundary conditions related to ice-volume and greenhouse-gas feedbacks. On the other hand, obliquity forcing of tropical climate has been shown to occur independently of high-latitude ice-sheet growth and decay as a result of interhemispheric insolation gradients (Bosmans et al., 2015), consistent with studies showing strong obliquity control on African monsoon runoff prior to the establishment of large northern hemispheric ice sheets (Zeeden et al., 2014; Lourens et al., 2001, 1996). It is important to note that whilst SAM expression above Site U1443 in the southern BOB is dominated by summer monsoon winds that drive surface ocean currents and deeper mixing, oceanographic conditions in the northern and eastern BOB (e.g. Sites U1447 and U1448) are instead primarily controlled by summer monsoon freshwater inputs (Jöhnck et al., 2020; Kuhnt et al., 2020). Runoff and direct precipitation during the SASM lead to strong salinity stratification in the northern parts of the BOB in the late summer and autumn, which prevents upper ocean mixing (e.g. Sengupta et al., 2016). These regional differences in the manifestation of the monsoon must be considered when interpreting records from the heterogeneous BOB, and records from multiple locations and proxies are needed to achieve a comprehensive picture of the SAM subsystem.

The 405 kyr eccentricity modulation of precession-scale export productivity variability broadly coincides with 405 kyr cycles in benthic δ^{13}C at Site U1443, with higher export productivity during benthic δ^{13}C minima and eccentricity maxima on these timescales (Fig. 10). Cross-spectral analysis indicates that log(Ba/Fe) and benthic δ^{13}C are > 95 % coherent at the ∼ 405 and 22–24 kyr periods, with an in-phase relationship in the precession band ($-13 \pm 25°$) and a near antiphase relationship on 405 kyr timescales ($151 \pm 27°$) (Fig. S4b). A 405 kyr modulation of the ocean carbon cycle, primarily recorded in carbonate content and benthic δ^{13}C records (Herbert, 1997; Drury et al., 2021; De Vleeschouwer et al., 2020; Westerhold et al., 2020; Pälike et al., 2012; Paillard, 2017; Holbourn et al., 2007) but also in productivity and monsoon-related dust records (Rickaby et al., 2007; Wang et al., 2010), has been observed throughout the Cenozoic and Mesozoic sedimentary record. In middle Miocene records, poor carbonate preservation noted during eccentricity maxima is interpreted in terms of transient shoaling of the carbonate saturation horizon (Holbourn et

al., 2007; Flower and Kennett, 1994). Here, we see a broad positive correlation between log(Ba/Fe) and log(Ca/Terr) records on 405 kyr timescales (Figs. 9a, b), suggesting that carbonate content fluctuations at Site U1443 in the late Miocene were more strongly related to biogenic production than to dissolution on long eccentricity timescales. The coincidence of late Miocene eccentricity maxima with productivity maxima and benthic $\delta^{13}C$ minima at Site U1443 is compatible with the hypothesis that a strengthened monsoon induced 405 kyr cycles in the marine carbon cycle via increased weathering and nutrient inputs during eccentricity maxima, leading to enhanced marine biological productivity and deep-ocean organic carbon burial (Ma et al., 2011).

5.3 Late Miocene monsoon evolution

On long timescales, our Site U1443 biogenic Ba records show relatively stable (9–6.5 Ma) or slightly decreasing (6.5–5.3 Ma) export productivity between 9 and 5 Ma (Figs. 7d–f, S7). Based on sediment colour properties and XRF-derived Ba/Ti ratios in the preceding interval (∼ 13.5–8.3 Ma), Lübbers et al. (2019) suggested that a shift towards a higher productivity regime occurred at ∼ 11.2 Ma at Site U1443, 2.5 Ma before the rise in $CaCO_3$ MAR at Site U1443 and also significantly earlier than the onset of the biogenic bloom at other sites (Farrell et al., 1995; Grant and Dickens, 2002; Dickens and Owen, 1999; Diester-Haass et al., 2005). Those authors also suggested that this shift was potentially linked to an intensification of the South Asian monsoon. An increase in export productivity at ∼ 11 Ma is consistent with long-term changes in benthic foraminiferal assemblages at Site 758 (Gupta et al., 2004; Nomura, 1995) and at sites in the western tropical Indian Ocean (Smart et al., 2007), as well as with opal records from the more remote equatorial Pacific (Lyle and Baldauf, 2015). Reconstructions of Arabian Sea upwelling, export productivity, and deoxygenation (Bialik et al., 2020; Gupta et al., 2015; Huang et al., 2007; Zhuang et al., 2017), as well as the abrupt appearance of drift sediments in the Maldives Archipelago at ∼ 13 Ma (Betzler et al., 2016), point towards an intensification of seasonally reversing South Asian monsoon winds between 13 and 11 Ma, consistent with Site U1443 export productivity records. Our new data suggest that similar levels of export productivity to those seen from 11.2 to 9 Ma persisted until at least 5 Ma at Site U1443.

Compiled Asian monsoon proxy records spanning the 9 to 5 Ma interval show relatively stable long-term SASM strength (Fig. 11; see Fig. 1c for site map). Similar to records from the Maldives and Arabian Sea (Tripathi et al., 2017; Huang et al., 2007; Betzler et al., 2016; Zhuang et al., 2017), Site U1443 records do not corroborate the hypothesis that SASM winds intensified at ∼ 8 to 7 Ma as suggested by some studies (Kroon et al., 1991; Singh and Gupta, 2014; Gupta et al., 2015; An et al., 2001).

The long-term trend in our record shows broad agreement with a low-resolution clay mineralogy record from Site U1447 in the Andaman Sea showing a gradual long-term decrease in smectite/(illite and chlorite) over the late Miocene (Fig. 11g), indicating strengthened physical weathering and/or weakened chemical weathering that can be attributed to the South Asian winter and summer monsoons respectively (Lee et al., 2020). Also at Site U1447, records of potassium content (%K, Fig. 11h) are interpreted to show a shift in sediment provenance and/or an increase in physical weathering and erosion in the sediment source region between ∼ 7 and ∼ 6 Ma (Fig. 11h), which may be linked to an increase in monsoon rainfall intensity and global cooling (Kuhnt et al., 2020). Between 6.2 and 5 Ma, our equatorial Indian Ocean wind records show good long-term agreement with a seawater $\delta^{18}O$ record from the Andaman Sea (Jöhnck et al., 2020), with a minimum in export productivity at ∼ 5.3 Ma at Site U1443 coinciding with a maximum in seawater $\delta^{18}O$ at Site U1448 (Fig. 11i, j). One interpretation of this could be a coupled reduction in both SASM wind intensity and runoff/precipitation over this interval, although Jöhnck et al. (2020) invoke an increase in local evaporation and/or a change in precipitation source to explain the decreasing seawater $\delta^{18}O$ values between 5.6 and 5.2 Ma. High-resolution records of precipitation and runoff from the SASM region further back in time are needed to verify to what extent monsoon winds and precipitation–runoff are coupled on long timescales.

In contrast to the relatively stable South Asian summer monsoon between 9 and 5 Ma, evidence for a step strengthening of the East Asian winter monsoon during the late Miocene (∼ 7 Ma) comes from the South China Sea (Holbourn et al., 2018; Wan et al., 2007) (Fig. 11a), whereas records from a site on the Chinese Loess Plateau suggest a more gradual intensification of the East Asian summer monsoon from 8.2 to 2.6 Ma (Ao et al., 2016) (Fig. 11b). The step change in South China Sea surface water geochemistry has been interpreted to reflect drying and cooling of the Asian interior and a related southward shift of the ITCZ (Inter-Tropical Convergence Zone) leading to an intensified dry winter monsoon over southeast Asia (Holbourn et al., 2018). An intensification of the East Asian winter monsoon around 7 Ma is consistent with an increase in aeolian dust delivery to the South China Sea at this time (Wan et al., 2007). The long-term increase in East Asian summer monsoon strength inferred from magnetic records in Chinese loess sequences is attributed to progressive Antarctic glaciation that drives an increased pressure gradient between the Australian High and Asian Low pressure cells, a mechanism supported by numerical simulations (Ao et al., 2016). However, a late Miocene intensification of the East Asian summer monsoon is not corroborated by studies from the South China Sea (Wan et al., 2007; Holbourn et al., 2021, 2018). The apparent insensitivity of equatorial SASM wind intensity to global late Miocene sea surface cooling, which began at ∼ 7.5 Ma and

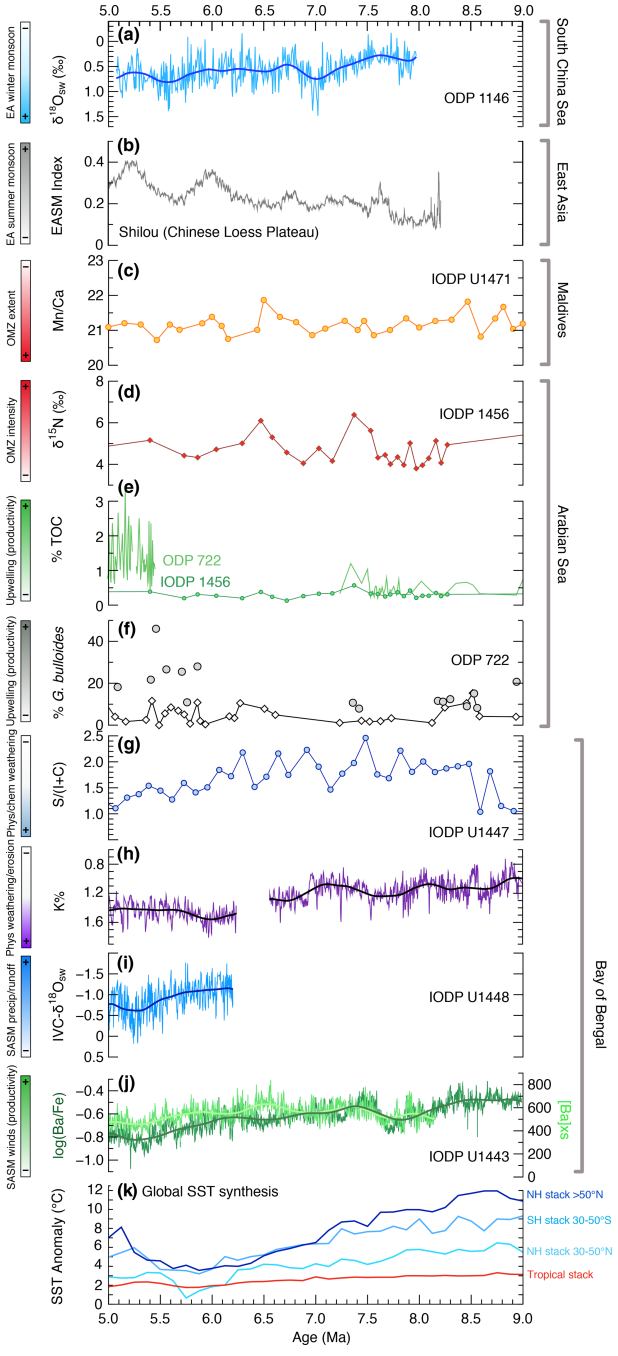

Figure 11. Compilation of late Miocene (9–5 Ma) Asian monsoon reconstructions, showing representative records from different regions and their published interpretations (bars on left). **(a)** Seawater $\delta^{18}O$ showing an increase in East Asian winter monsoon strength at ~ 7.4 Ma (Holbourn et al., 2018, 2021); **(b)** stacked magnetic records of the East Asian summer monsoon from the Chinese Loess Plateau (Ao et al., 2016); **(c)** Mn/Ca ratios used to trace oxygen minimum zone (OMZ) variations from Maldives Site IODP U1471 (Betzler et al., 2016); **(d)** $\delta^{15}N$ record from Arabian Sea site IODP U1456 showing OMZ intensity (Tripathi et al., 2017); **(e)** total organic carbon (TOC) % from Arabian Sea sites IODP U1456 and ODP Site 722 (Huang et al., 2007; Tripathi et al., 2017); **(f)** % *Gobigerinoides bulloides*, a planktic foraminiferal upwelling indicator, at ODP Site 722 (Huang et al., 2007; Kroon et al., 1991), *G. bulloides* was counted in the > 150 µm fraction in Huang et al. (2007) (white diamonds) and the > 125 µm fraction in Kroon et al. (1991) (grey circles); **(g)** clay mineralogy (smectite/(illite+ chlorite)) at IODP Site U1447 in the Andaman Sea (Lee et al., 2020); **(h)** percentage of potassium (K%) at IODP Site U1447 derived from spectral natural gamma ray measurements (Kuhnt et al., 2020); **(i)** Andaman Sea IODP Site U1448 ice-volume-corrected seawater $\delta^{18}O$ record (Jöhnck et al., 2020); and **(j)** export productivity records from Site U1443 (this study). **(k)** Global sea surface temperature trends (expressed as anomalies relative to the present), stacked by latitude band (Herbert et al., 2016). All records are on their original age models, and Loess smooths are shown for high-resolution records.

culminated in an SST minimum at ∼ 6 Ma (Fig. 11k) (Herbert et al., 2016), is consistent with climate modelling studies that show limited impact of different pCO_2 scenarios on SASM wind patterns and strength (Kitoh et al., 1997). The South Asian summer monsoon has been described as a thermally direct circulation driven by the thermal contrast between the Indian subcontinent and the equatorial Indian Ocean that develops in summer, with abrupt transitions between summer and winter monsoon regimes suggested to be related to feedbacks between extratropical eddies and tropical circulation (Privé and Plumb, 2007a, b; Lutsko et al., 2019; Bordoni and Schneider, 2008; Geen et al., 2018). Changes in the cross-equatorial temperature gradient have been shown to substantially impact the strength of onshore SASM monsoon flow (Lutsko et al., 2019; Acosta and Huber, 2020). The lack of a long-term trend in wind and surface circulation proxies over the 9 to 5 Ma interval (Fig. 11) suggests a relatively constant land–sea temperature gradient despite global cooling. Thus, although single-site records may not be representative of the East or South Asian monsoon subsystems as a whole our data add to the body of evidence suggesting decoupling between the East Asian and South Asian monsoons on long timescales.

6 Summary and conclusions

We present new equatorial Indian Ocean benthic $\delta^{13}C$ and $\delta^{18}O$ records and an age model spanning the interval between 9 and 5 Ma (late Miocene–earliest Pliocene) and analyse sedimentation and productivity trends and cyclicity using XRF-derived records and MARs. Biogenic sediment MARs reveal a modest imprint of the late Miocene biogenic bloom at Site U1443 lasting until at least 5 Ma, primarily driven by fine-fraction (coccolith) $CaCO_3$ accumulation, as noted at other sites (Si and Rosenthal, 2019). Nevertheless, the carbonate MAR record of Site U1443 is clearly influenced by carbonate preservation as well as production over the late Miocene, so independent productivity proxies must be considered when defining the duration of the biogenic bloom. Our results indicate that step increases in sediment accumulation rate recorded on the Ninetyeast Ridge at ∼ 9–8 Ma primarily reflect an increase in $CaCO_3$ accumulation, and that this is likely independent from the increase in lithogenic sediment flux recorded in nearby Nicobar Fan sites, itself related to sediment re-routing within the Nicobar–Bengal Fan system around the same time (McNeill et al., 2017; Pickering et al., 2020a). Our data show no long-term increase in export productivity between 9 and 5 Ma (and by inference no intensification of SASM winds); therefore these data support existing evidence for an early late Miocene (∼ 13–10 Ma) establishment of strong seasonally reversing South Asian monsoon winds and Arabian Sea upwelling, with relatively stable or slightly weakening SASM winds over the remainder of the late Miocene and earliest Pliocene between 9 and 5 Ma. Spectral and cross-spectral analyses of XRF-based biogenic barium records reveal that export productivity in waters overlying Site U1443 was consistently paced by precession, with amplitude modulation of the precession signal on ∼ 405 kyr timescales and no significant variability at glacial–interglacial (obliquity) timescales. Coeval late Miocene productivity maxima and benthic $\delta^{13}C$ minima during eccentricity maxima at Site U1443 provide support for the hypothesis that the monsoon may have paced changes in the carbon cycle on ∼ 405 kyr timescales (Ma et al., 2011). Significant coherence and an in-phase relationship at the precession band between biogenic barium and the SITIG suggest direct forcing of South Asian monsoon winds by insolation gradients over the late Miocene, relatively unaffected by glacial boundary conditions and long-term global cooling trends (Herbert et al., 2016). In contrast, East Asian summer and winter monsoons appear to have intensified during the late Miocene in response to global cooling and Antarctic ice sheet growth and related feedbacks (Ao et al., 2016; Holbourn et al., 2018), although more continuous records over the late Miocene are needed to understand regional trends due to the heterogeneous nature of Asian monsoon expression.

Data availability. All data are available on the PANGAEA database at https://doi.org/10.1594/PANGAEA.935166 (Bolton et al., 2021).

Supplement. The supplement related to this article is available online at: https://doi.org/10.5194/cp-18-713-2022-supplement.

Author contributions. CTB designed the study. Sample processing and picking of benthic foraminifera was carried out by EG and CTB. Picked foraminifera samples were verified and cleaned by AH, WK, and JL, and stable isotopes measurements were performed by NA, AH, WK, and JL. XRF scanning was carried out by CTB in collaboration with KG, GM, and EJR. XRF calibration was carried out by EG and KT. The paper was written by CTB with feedback from all authors. ACS contributed to discussions and data interpretation.

Competing interests. The contact author has declared that neither they nor their co-authors have any competing interests.

Disclaimer. Publisher's note: Copernicus Publications remains neutral with regard to jurisdictional claims in published maps and institutional affiliations.

Acknowledgements. This research used samples and data provided by the International Ocean Discovery Program (IODP). We

thank the science party, technical staff, and crew of IODP Expedition 353. The authors acknowledge the financial support provided by French ANR, IODP France, and Deutsche Forschungsgemeinschaft. Katharine Grant acknowledges financial support from the Australian Research Council. Clara T. Bolton thanks Anna Joy Drury and Tim Herbert for age model feedback, and Luc Beaufort, Baptiste Suchéras-Marx, and Ian Bailey for discussions that helped improve the paper. Marta Garcia Molina, Jean-Charles Mazur, and Christine Pailles are thanked for technical laboratory support at CEREGE.

Financial support. This research has been supported by the Agence Nationale de la Recherche project iMonsoon (grant no. ANR-16-CE01-0004-01), the Deutsche Forschungsgemeinschaft (grant no. Ku649/36-1), IODP France, and Australian Research Council (grant no. DE190100042).

Review statement. This paper was edited by Arne Winguth and reviewed by David De Vleeschouwer and Mitch Lyle.

References

Acosta, R. and Huber, M.: Competing topographic mechanisms for the summer Indo-Asian monsoon, Geophys. Res. Lett., 47, e2019GL085112, https://doi.org/10.1029/2019GL085112, 2020.

Ali, S., Hathorne, E., and Frank, M.: Persistent provenance of South Asian Monsoon induced silicate weathering over the past 27 million years, Paleoceanography and Paleoclimatology, 36, e2020PA003909. https://doi.org/10.1029/2020PA003909, 2021.

An, Z., Kutzbach, J. E., Prell, W. L., and Porter, S. C.: Evolution of Asian monsoons and phased uplift of the Himalaya–Tibetan plateau since Late Miocene times, Nature, 411, 62–66, 2001.

An, Z., Clemens, S. C., Shen, J., Qiang, X., Jin, Z., Sun, Y., Prell, W. L., Luo, J., Wang, S., and Xu, H.: Glacial-interglacial Indian summer monsoon dynamics, Science, 333, 719–723, 2011.

Ao, H., Roberts, A. P., Dekkers, M. J., Liu, X., Rohling, E. J., Shi, Z., An, Z., and Zhao, X.: Late Miocene–Pliocene Asian monsoon intensification linked to Antarctic ice-sheet growth, Earth Planet. Sc. Lett., 444, 75–87, 2016.

Averyt, K. B. and Paytan, A.: A comparison of multiple proxies for export production in the equatorial Pacific, Paleoceanography, 19, PA4003, https://doi.org/10.1029/2004PA001005, 2004.

Behrenfeld, M. J. and Falkowski, P. G.: Photosynthetic rates derived from satellite-based chlorophyll concentration, Limnol. Oceanogr., 42, 1–20, 1997.

Behrenfeld, M. J., Boss, E., Siegel, D. A., and Shea, D. M.: Carbon-based ocean productivity and phytoplankton physiology from space, Global Biogeochem. Cy., 19, GB1006, https://doi.org/10.1029/2004GB002299, 2005.

Betzler, C., Eberli, G. P., Kroon, D., Wright, J. D., Swart, P. K., Nath, B. N., Alvarez-Zarikian, C. A., Alonso-García, M., Bialik, O. M., and Blättler, C. L.: The abrupt onset of the modern South Asian Monsoon winds, Scientific reports, 6, 29838, https://doi.org/10.1038/srep29838, 2016.

Betzler, C., Eberli, G., Lüdmann, T., Reolid, J., Kroon, D., Reijmer, J., Swart, P., Wright, J., Young, J., and Alvarez-Zarikian, C.: Refinement of Miocene sea level and monsoon events from the sedimentary archive of the Maldives (Indian Ocean), Progress in Earth and Planetary Science, 5, 1–18, 2018.

Bialik, O. M., Auer, G., Ogawa, N. O., Kroon, D., Waldmann, N. D., and Ohkouchi, N.: Monsoons, upwelling, and the deoxygenation of the northwestern Indian Ocean in response to middle to late Miocene global climatic shifts, Paleoceanography and Paleoclimatology, 35, e2019PA003762. https://doi.org/10.1029/2019PA003762, 2020.

Bickert, T., Haug, G., and Tiedemann, R.: Late Neogene benthic stable isotope record of ODP Site 999: Implications for Caribbean paleoceanography, organic carbon burial and the Messinian Salinity Crisis, Paleoceanography, 19, PA1023, https://doi.org/10.1029/2002PA000799, 2004.

Bishop, J. K.: The barite-opal-organic carbon association in oceanic particulate matter, Nature, 332, 341–343, 1988.

Bolton, C. T., Chang, L., Clemens, S. C., Kodama, K., Ikehara, M., Medina-Elizalde, M., Paterson, G. A., Roberts, A. P., Rohling, E. J., and Yamamoto, Y.: A 500,000 year record of Indian summer monsoon dynamics recorded by eastern equatorial Indian Ocean upper water-column structure, Quaternary Sci. Rev., 77, 167–180, https://doi.org/10.1016/j.quascirev.2013.07.031, 2013.

Bolton, C. T., Gray, E., Kuhnt, W., Holbourn, A., Lübbers, J., Grant, K. M., Tachikawa, K., Marino, G., Rohling, E. J., Sarr, A.-C., and Andersen, N.: Late Miocene benthic stable isotope data, age model, and X-Ray Fluorescence data from IODP Site U1443, equatorial Indian Ocean, PANGAEA [data set], https://doi.org/10.1594/PANGAEA.935166, 2021.

Boos, W. R. and Kuang, Z.: Dominant control of the South Asian monsoon by orographic insulation versus plateau heating, Nature, 463, 218–222, 2010.

Bordoni, S. and Schneider, T.: Monsoons as eddy-mediated regime transitions of the tropical overturning circulation, Nat. Geosci., 1, 515–519, 2008.

Bosmans, J., Erb, M., Dolan, A., Drijfhout, S., Tuenter, E., Hilgen, F., Edge, D., Pope, J. O., and Lourens, L.: Response of the Asian summer monsoons to idealized precession and obliquity forcing in a set of GCMs, Quaternary Sci. Rev., 188, 121–135, 2018.

Bosmans, J. H. C., Hilgen, F. J., Tuenter, E., and Lourens, L. J.: Obliquity forcing of low-latitude climate, Clim. Past, 11, 1335–1346, https://doi.org/10.5194/cp-11-1335-2015, 2015.

Bretschneider, L., Hathorne, E. C., Bolton, C. T., Gebregiorgis, D., Giosan, L., Gray, E., Huang, H., Holbourn, A., Kuhnt, W., and Frank, M.: Enhanced late Miocene chemical weathering and altered precipitation patterns in the watersheds of the Bay of Bengal recorded by detrital clay radiogenic isotopes, Paleoceanography and Paleoclimatology, 36, e2021PA004252, https://doi.org/10.1029/2021PA004252, 2021.

Bukry, D.: Coccolith and silicoflagellate stratigraphy, eastern Indian Ocean, Deep Sea Drilling Project Leg 22, in: Initial Reports of the Deep Sea Drilling Project, edited by: Pimm, A. C., Washington, https://doi.org/10.2973/dsdp.proc.22.127.1974, 1974.

Caley, T., Malaizé, B., Zaragosi, S., Rossignol, L., Bourget, J., Eynaud, F., Martinez, P., Giraudeau, J., Charlier, K., and Ellouz-Zimmermann, N.: New Arabian Sea records help decipher orbital timing of Indo-Asian monsoon, Earth Planet. Sc. Lett., 308, 433–444, https://doi.org/10.1016/j.epsl.2011.06.019, 2011.

Cao, Z., Siebert, C., Hathorne, E. C., Dai, M., and Frank, M.: Constraining the oceanic barium cycle with stable barium isotopes, Earth Planet. Sc. Lett., 434, 1–9, 2016.

Clemens, S. C. and Prell, W. L.: Late Pleistocene variability of Arabian Sea summer monsoon winds and continental aridity: Eolian records from the lithogenic component of deep-sea sediments, Paleoceanography, 5, 109–145, 1990.

Clemens, S. C. and Prell, W. L.: A 350,000 year summer-monsoon multi-proxy stack from the Owen Ridge, Northern Arabian Sea, Mar. Geol., 201, 35–51, https://doi.org/10.1016/S0025-3227(03)00207-X, 2003.

Clemens, S. C., Prell, W., Murray, D., Shimmield, G., and Weedon, G.: Forcing mechanisms of the Indian Ocean monsoon, Nature, 353, 720–725, https://doi.org/10.1038/353720a0, 1991.

Clemens, S. C., Prell, W. L., and Sun, Y.: Orbital-scale timing and mechanisms driving Late Pleistocene Indo-Asian summer monsoons: Reinterpreting cave speleothem δ18O, Paleoceanography, 25, PA4207, https://doi.org/10.1029/2010PA001926, 2010.

Clemens, S. C., Kuhnt, W., LeVay, L. J., Anand, P., Ando, T., Bartol, M., Bolton, C. T., Ding, X., Gariboldi, K., Giosan, L., Hathorne, E., Huang, Y., Jaiswal, P., Kim, S., Kirkpatrick, J. B., Littler, K., Marino, G., Martinez, P., Naik, D., Peketi, A., Phillips, S. C., Robinson, M. M., Romero, O. E., Sagar, N., Taladay, K., Taylor, S. N., Thirumalai, K., Uramoto, G., Y. Usui, Wang, J., Yamamoto, M., and Zhou, L.: Site U1443, in: Indian Monsoon Rainfall. Proceedings of the International Ocean Discovery Program, edited by: Clemens, S. C., Kuhnt, W., LeVay, L. J., and the Expedition 353 Scientists, College Station, TX (International Ocean Discovery Program), https://doi.org/10.14379/iodp.proc.353.103.2016, 2016.

Clemens, S. C., Holbourn, A., Kubota, Y., Lee, K., Liu, Z., Chen, G., Nelson, A., and Fox-Kemper, B.: Precession-band variance missing from East Asian monsoon runoff, Nat. Commun., 9, 1–12, 2018.

Clemens, S. C., Yamamoto, M., Thirumalai, K., Giosan, L., Richey, J. N., Nilsson-Kerr, K., Rosenthal, Y., Anand, P., and McGrath, S. M.: Remote and local drivers of Pleistocene South Asian summer monsoon precipitation: A test for future predictions, Science Advances, 7, eabg3848, https://doi.org/10.1126/sciadv.abg3848, 2021.

Clift, P. D. and Webb, A. A. G.: A history of the Asian monsoon and its interactions with solid Earth tectonics in Cenozoic South Asia, Geological Society, London, Special Publications, 483, 631–652, 2019.

Clift, P. D., Hodges, K. V., Heslop, D., Hannigan, R., Van Long, H., and Calves, G.: Correlation of Himalayan exhumation rates and Asian monsoon intensity, Nat. Geosci., 1, 875–880, 2008.

Dehairs, F., Chesselet, R., and Jedwab, J.: Discrete suspended particles of barite and the barium cycle in the open ocean, Earth Planet. Sc. Lett., 49, 528–550, 1980.

Delaney, M. L. and Filippelli, G. M.: An apparent contradiction in the role of phosphorus in Cenozoic chemical mass balances for the world ocean, Paleoceanography, 9, 513–527, 1994.

De Vleeschouwer, D., Drury, A. J., Vahlenkamp, M., Rochholz, F., Liebrand, D., and Pälike, H.: High-latitude biomes and rock weathering mediate climate–carbon cycle feedbacks on eccentricity timescales, Nat. Commun., 11, 1–10, 2020.

Dickens, G. R. and Owen, R. M.: The latest Miocene–early Pliocene biogenic bloom: a revised Indian Ocean perspective, Mar. Geol., 161, 75–91, 1999.

Diester-Haass, L., Billups, K., and Emeis, K. C.: In search of the late Miocene–early Pliocene "biogenic bloom" in the Atlantic Ocean (Ocean Drilling Program Sites 982, 925, and 1088), Paleoceanography, 20, PA4001, https://doi.org/10.1029/2005PA001139, 2005.

Diester-Haass, L., Billups, K., and Emeis, K. C.: Late Miocene carbon isotope records and marine biological productivity: Was there a (dusty) link?, Paleoceanography, 21, PA4216, https://doi.org/10.1029/2006PA001267, 2006.

Ding, Z., Huang, G., Liu, F., Wu, R., and Wang, P.: Responses of global monsoon and seasonal cycle of precipitation to precession and obliquity forcing, Clim. Dynam., 56, 3733–3747, 2021.

Drury, A. J., John, C. M., and Shevenell, A. E.: Evaluating climatic response to external radiative forcing during the late Miocene to early Pliocene: New perspectives from eastern equatorial Pacific (IODP U1338) and North Atlantic (ODP 982) locations, Paleoceanography, 31, 167–184, 2016.

Drury, A. J., Westerhold, T., Frederichs, T., Tian, J., Wilkens, R., Channell, J. E., Evans, H., John, C. M., Lyle, M., and Röhl, U.: Late Miocene climate and time scale reconciliation: Accurate orbital calibration from a deep-sea perspective, Earth Planet. Sc. Lett., 475, 254–266, 2017.

Drury, A. J., Lee, G., Gray, W., Lyle, M., Westerhold, T., Shevenell, A. E., and John, C.: Deciphering the state of the late Miocene to early Pliocene equatorial Pacific, Paleoceanography and Paleoclimatology, 33, 246–263, 2018.

Drury, A. J., Liebrand, D., Westerhold, T., Beddow, H. M., Hodell, D. A., Rohlfs, N., Wilkens, R. H., Lyle, M., Bell, D. B., Kroon, D., Pälike, H., and Lourens, L. J.: Climate, cryosphere and carbon cycle controls on Southeast Atlantic orbital-scale carbonate deposition since the Oligocene (30–0 Ma), Clim. Past, 17, 2091–2117, https://doi.org/10.5194/cp-17-2091-2021, 2021.

Dymond, J., Suess, E., and Lyle, M.: Barium in deep-sea sediment: A geochemical proxy for paleoproductivity, Paleoceanography, 7, 163–181, 1992.

Eagle, M., Paytan, A., Arrigo, K. R., van Dijken, G., and Murray, R. W.: A comparison between excess barium and barite as indicators of carbon export, Paleoceanography, 18, 1021, https://doi.org/10.1029/2002PA000793 2003.

ERD, NOAA, NMFS, and SWFSC: Primary Productivity, Aqua MODIS, NPP, Global, 2003-present, EXPERIMENTAL (Monthly Composite), erdMH1ppmday, ERDDAP, https://coastwatch.pfeg.noaa.gov/erddap/griddap/erdMH1ppmday.html, last access: 28 September 2020.

Farnsworth, A., Lunt, D. J., Robinson, S. A., Valdes, P. J., Roberts, W. H., Clift, P. D., Markwick, P., Su, T., Wrobel, N., and Bragg, F.: Past East Asian monsoon evolution controlled by paleogeography, not CO_2, Science Advances, 5, eaax1697, https://doi.org/10.1126/sciadv.aax1697, 2019.

Farrell, J. W., Raffi, I., Janecek, T. R., Murray, D. W., Levitan, M., Dadey, K. A., Emeis, K.-C., Lyle, M., Flores, J.-A., and Hovan, S.: Late Neogene sedimentation patterns in the eastern equatorial Pacific Ocean, in: Proc. ODProgram, edited by: Pisias, N. G., Mayer, L. A., Janecek, T. R., Palmer-Julson, A., and van Andel, T. H., Scientific Results, 138, 717–756, 1995.

Flower, B. P. and Kennett, J. P.: The middle Miocene climatic transition: East Antarctic ice sheet development, deep ocean circulation and global carbon cycling, Palaeogeogr. Palaeocl., 108, 537–555, 1994.

Fox, B. R., D'Andrea, W., Wilson, G., Lee, D., and Wartho, J.-A.: Interaction of polar and tropical influences in the mid-latitudes of the Southern Hemisphere during the Mi-1 deglaciation, Global Planet. Change, 155, 109–120, 2017.

Francois, R., Honjo, S., Manganini, S. J., and Ravizza, G. E.: Biogenic barium fluxes to the deep sea: Implications for paleoproductivity reconstruction, Global Biogeochem. Cy., 9, 289–303, 1995.

Gadgil, S.: The Indian monsoon and its variability, Annu. Rev. Earth Pl. Sc., 31, 429–467, 2003.

Gebregiorgis, D., Hathorne, E. C., Giosan, L., Clemens, S., Nürnberg, D., and Frank, M.: Southern Hemisphere forcing of South Asian monsoon precipitation over the past ∼ 1 million years, Nat. Commun., 9, 4702, https://doi.org/10.1038/s41467-018-07076-2, 2018.

Geen, R., Lambert, F., and Vallis, G.: Regime change behavior during Asian monsoon onset, J. Climate, 31, 3327–3348, 2018.

Gingele, F. and Dahmke, A.: Discrete barite particles and barium as tracers of paleoproductivity in South Atlantic sediments, Paleoceanography, 9, 151–168, 1994.

Goldberg, E. D. and Arrhenius, G.: Chemistry of Pacific pelagic sediments, Geochim. Cosmochim. Ac., 13, 153–212, 1958.

Gonneea, M. E. and Paytan, A.: Phase associations of barium in marine sediments, Mar. Chem., 100, 124–135, 2006.

Goswami, B., Krishnamurthy, V., and Annmalai, H.: A broad-scale circulation index for the interannual variability of the Indian summer monsoon, Q. J. Roy. Meteor. Soc., 125, 611–633, 1999.

Gouhier, T. C., Grinsted, A., and Simko, V.: R package biwavelet: Conduct Univariate and Bivariate Wavelet Analyses, Version 0.20.17, GitHub, https://github.com/tgouhier/biwavelet (last access: August 2020), 2018.

Gradstein, F. M., Ogg, J. G., Schmitz, M. B., and Ogg, G. M.: The geologic time scale 2012, Elsevier, ISBN: 978-0-44-459390-0, 2012.

Grant, K. M. and Dickens, G. R.: Coupled productivity and carbon isotope records in the southwest Pacific Ocean during the late Miocene–early Pliocene biogenic bloom, Palaeogeogr. Palaeocl., 187, 61–82, 2002.

Grinsted, A., Moore, J. C., and Jevrejeva, S.: Application of the cross wavelet transform and wavelet coherence to geophysical time series, Nonlin. Processes Geophys., 11, 561–566, https://doi.org/10.5194/npg-11-561-2004, 2004.

Guo, Z., Ruddiman, W. F., Hao, Q., Wu, H., Qiao, Y., Zhu, R. X., Peng, S., Wei, J., Yuan, B., and Liu, T.: Onset of Asian desertification by 22 Myr ago inferred from loess deposits in China, Nature, 416, 159–163, 2002.

Gupta, A. K., Singh, R. K., Joseph, S., and Thomas, E.: Indian Ocean high-productivity event (10–8 Ma): Linked to global cooling or to the initiation of the Indian monsoons?, Geology, 32, 753–756, 2004.

Gupta, A. K., Yuvaraja, A., Prakasam, M., Clemens, S. C., and Velu, A.: Evolution of the South Asian monsoon wind system since the late Middle Miocene, Palaeogeogr. Palaeocl., 438, 160–167, 2015.

Herbert, T. D.: A long marine history of carbon cycle modulation by orbital-climatic changes, P. Natl. Acad. Sci. USA, 94, 8362–8369, 1997.

Herbert, T. D., Lawrence, K. T., Tzanova, A., Peterson, L. C., Caballero-Gill, R., and Kelly, C. S.: Late Miocene global cooling and the rise of modern ecosystems, Nat. Geosci., 9, 843–847, https://doi.org/10.1038/ngeo2813, 2016.

Hermoyian, C. S. and Owen, R. M.: Late Miocene-early Pliocene biogenic bloom: Evidence from low-productivity regions of the Indian and Atlantic Oceans, Paleoceanography, 16, 95–100, 2001.

Holbourn, A., Kuhnt, W., Schulz, M., Flores, J.-A., and Andersen, N.: Orbitally-paced climate evolution during the middle Miocene "Monterey" carbon-isotope excursion, Earth Planet. Sc. Lett., 261, 534–550, 2007.

Holbourn, A., Kuhnt, W., Clemens, S. C., Kochhann, K. G., Jöhnck, J., Lübbers, J., and Andersen, N.: Late Miocene climate cooling and intensification of southeast Asian winter monsoon, Nat. Commun., 9, 1584, https://doi.org/10.1038/s41467-018-03950-1, 2018.

Holbourn, A., Kuhnt, W., Clemens, S. C., and Heslop, D.: A ∼ 12 Myr Miocene record of East Asian Monsoon variability from the South China Sea, Paleoceanography and Paleoclimatology, 36, e2021PA004267, https://doi.org/10.1029/2021PA004267, 2021.

Hovan, S. A. and Rea, D. K.: The Cenozoic record of continental mineral deposition on Broken and Ninetyeast Ridges, Indian Ocean: southern African aridity and sediment delivery from the Himalayas, Paleoceanography, 7, 833–860, 1992.

Howell, P., Pisias, N., Ballance, J. Baughman, J., and Ochs, L.: ARAND Time-Series Analysis Software, Brown University, Providence, RI, GitHub, https://github.com/jesstierney/arand (last access: 27 November 2018), 2006.

Huang, Y., Clemens, S. C., Liu, W., Wang, Y., and Prell, W. L.: Large-scale hydrological change drove the late Miocene C_4 plant expansion in the Himalayan foreland and Arabian Peninsula, Geology, 35, 531–534, https://doi.org/10.1130/G23666A.1, 2007.

Jalihal, C., Bosmans, J. H. C., Srinivasan, J., and Chakraborty, A.: The response of tropical precipitation to Earth's precession: the role of energy fluxes and vertical stability, Clim. Past, 15, 449–462, https://doi.org/10.5194/cp-15-449-2019, 2019.

Jensen, T. G.: Cross-equatorial pathways of salt and tracers from the northern Indian Ocean: Modelling results, Deep-Sea Res. Pt. II, 50, 2111–2127, 2003.

Jia, G., Peng, P. A., Zhao, Q., and Jian, Z.: Changes in terrestrial ecosystem since 30 Ma in East Asia: Stable isotope evidence from black carbon in the South China Sea, Geology, 31, 1093–1096, 2003.

Jöhnck, J., Kuhnt, W., Holbourn, A., and Andersen, N.: Variability of the Indian Monsoon in the Andaman Sea across the Miocene-Pliocene transition, Paleoceanography and Paleoclimatology, 35, e2020PA003923, https://doi.org/10.1029/2020PA003923, 2020.

Jöhnck, J., Holbourn, A. E., Kuhnt, W., and Andersen, N.: Oxygen isotope offsets in deep-water benthic foraminifera, J. Foramin. Res., 51, 225–244, 2021.

Jyothibabu, R., Vinayachandran, P., Madhu, N., Robin, R., Karnan, C., Jagadeesan, L., and Anjusha, A.: Phytoplankton size structure in the southern Bay of Bengal modified by the Summer Monsoon

Current and associated eddies: Implications on the vertical biogenic flux, J. Marine Syst., 143, 98–119, 2015.

Kathayat, G., Cheng, H., Sinha, A., Spötl, C., Edwards, R. L., Zhang, H., Li, X., Yi, L., Ning, Y., and Cai, Y.: Indian monsoon variability on millennial-orbital timescales, Scientific Reports, 6, 24374, https://doi.org/10.1038/srep24374, 2016.

Keerthi, M., Lengaigne, M., Vialard, J., de Boyer Montégut, C., and Muraleedharan, P.: Interannual variability of the Tropical Indian Ocean mixed layer depth, Clim. Dynam., 40, 743–759, 2013.

Keigwin, L.: Late Cenozoic stable isotope stratigraphy and paleoceanography of DSDP sites from the east equatorial and central North Pacific Ocean, Earth Planet. Sc. Lett., 45, 361–382, 1979.

Keigwin, L. and Shackleton, N.: Uppermost Miocene carbon isotope stratigraphy of a piston core in the equatorial Pacific, Nature, 284, 613–614, 1980.

Kitoh, A., Yukimoto, S., Noda, A., and Motoi, T.: Simulated changes in the Asian summer monsoon at times of increased atmospheric CO_2, J. Meteorol. Soc. Jpn., Ser. II, 75, 1019–1031, 1997.

Koné, V., Aumont, O., Lévy, M., and Resplandy, L.: Physical and biogeochemical controls of the phytoplankton seasonal cycle in the Indian Ocean: A modeling study, in: Indian Ocean Biogeochemical Processes and Ecological Variability, edited by: Wiggert, J. D., Hood, Raleigh, R., Naqvi, S. W. A., Brink, K. H., Smith, S. L., Geophysical Monograph Series, 185, 147–166, https://doi.org/10.1029/2008GM000700, 2009.

Kroon, D., Steens, T., and Troelstra, S. R.: 13. Onset of Monsoonal Related Upwelling in the Western Arabian Sea as Revealed by Planktonic Foraminifers, in Proc. ODP, College Station, TX (Ocean Drilling Program), edited by: Emeis, K.-C., Meyers, P. A., Niitsuma, M., and Prell, W. L., Scientific Results, 117, 257–263, https://doi.org/10.2973/odp.proc.sr.117.1991, 1991.

Kuhnt, W., Holbourn, A. E., Jöhnck, J., and Lübbers, J.: Miocene to Pleistocene Palaeoceanography of the Andaman Region: Evolution of the Indian Monsoon on a Warmer-Than-Present Earth, in: The Andaman Islands and Adjoining Offshore: Geology, Tectonics and Palaeoclimate, Society of Earth Scientists Series, Springer, 261–288, https://doi.org/10.1007/978-3-030-39843-9, 2020.

Kutzbach, J. E.: Monsoon climate of the early Holocene: climate experiment with the earth's orbital parameters for 9000 years ago, Science, 214, 59–61, 1981.

Laskar, J., Robutel, P., Joutel, F., Gastineau, M., Correia, A. C. M., and Levrard, B.: A long-term numerical solution for the insolation quantities of the Earth, Astron. Astrophys., 428, 261–285, 2004.

Le, J. and Shackleton, N. J.: Carbonate dissolution fluctuations in the western equatorial Pacific during the late Quaternary, Paleoceanography, 7, 21–42, 1992.

Lee, J., Kim, S., Lee, J. I., Cho, H. G., Phillips, S. C., and Khim, B.-K.: Monsoon-influenced variation of clay mineral compositions and detrital Nd-Sr isotopes in the western Andaman Sea (IODP Site U1447) since the late Miocene, Palaeogeogr. Palaeocl., 538, 109339, https://doi.org/10.1016/j.palaeo.2019.109339, 2020.

Lévy, M., Shankar, D., André, J. M., Shenoi, S., Durand, F., and de Boyer Montégut, C.: Basin-wide seasonal evolution of the Indian Ocean's phytoplankton blooms, J. Geophys. Res., 112, C12014, https://doi.org/10.1029/2007JC004090, 2007.

Li, M., Hinnov, L., and Kump, L.: Acycle: Time-series analysis software for paleoclimate research and education, Comput. Geosci., 127, 12–22, https://doi.org/10.1016/j.cageo.2019.02.011, 2019.

Licht, A., Van Cappelle, M., Abels, H., Ladant, J.-B., Trabucho-Alexandre, J., France-Lanord, C., Donnadieu, Y., Vandenberghe, J., Rigaudier, T., and Lécuyer, C.: Asian monsoons in a late Eocene greenhouse world, Nature, 513, 501–506, 2014.

Longhurst, A.: Seasonal cycles of pelagic production and consumption, Prog. Oceanogr., 36, 77–167, 1995.

Lourens, L. J., Antonarakou, A., Hilgen, F., Van Hoof, A. A. M., Vergnaud-Grazzini, C., and Zachariasse, W. J.: Evaluation of the Plio-Pleistocene astronomical timescale, Paleoceanography, 11, 391–413, https://doi.org/10.1029/96pa01125, 1996.

Lourens, L. J., Wehausen, R., and Brumsack, H. J.: Geological constraints on tidal dissipation and dynamical ellipticity of the Earth over the past three million years, Nature, 409, 1029–1033, 2001.

Lübbers, J., Kuhnt, W., Holbourn, A. E., Bolton, C. T., Gray, E., Usui, Y., Kochhann, K. G., Beil, S., and Andersen, N.: The middle to late Miocene "Carbonate Crash" in the equatorial Indian Ocean, Paleoceanography and Paleoclimatology, 34, 813–832, 2019.

Lutsko, N. J., Marshall, J., and Green, B.: Modulation of monsoon circulations by cross-equatorial ocean heat transport, J. Climate, 32, 3471–3485, 2019.

Lyle, M. and Baldauf, J.: Biogenic sediment regimes in the Neogene equatorial Pacific, IODP Site U1338: Burial, production, and diatom community, Palaeogeogr. Palaeocl., 433, 106–128, 2015.

Ma, W., Tian, J., Li, Q., and Wang, P.: Simulation of long eccentricity (400-kyr) cycle in ocean carbon reservoir during Miocene Climate Optimum: Weathering and nutrient response to orbital change, Geophys. Res. Lett., 38, L10701, https://doi.org/10.1029/2011GL047680, 2011.

Martínez-Ruiz, F., Paytan, A., Gonzalez-Muñoz, M., Jroundi, F., Abad, M. d. M., Lam, P. J., Bishop, J., Horner, T., Morton, P. L., and Kastner, M.: Barite formation in the ocean: Origin of amorphous and crystalline precipitates, Chem. Geol., 511, 441–451, 2019.

McCreary, J., Murtugudde, R., Vialard, J., Vinayachandran, P., Wiggert, J. D., Hood, R. R., Shankar, D., and Shetye, S.: Biophysical processes in the Indian Ocean, in: Indian Ocean biogeochemical processes and ecological variability, edited by: McCreary, J. P., Murtugudde, R., Vialard, J., Vinayachandran, P. N., Wiggert, J. D., Hood, R. R., Shankar, D., and Shetye, S., Geophysical Monograph Series, 185, 9–32, https://doi.org/10.1029/2008GM000768, 2009.

McLennan, S. M.: Relationships between the trace element composition of sedimentary rocks and upper continental crust, Geochem. Geophy. Geosy., 2, 1021, https://doi.org/10.1029/2000GC000109, 2001.

McNeill, L. C., Dugan, B., Backman, J., Pickering, K. T., Pouderoux, H. F., Henstock, T. J., Petronotis, K. E., Carter, A., Chemale Jr., F., and Milliken, K. L.: Understanding Himalayan erosion and the significance of the Nicobar Fan, Earth Planet. Sc. Lett., 475, 134–142, 2017.

Meyers, S. R.: Astrochron: An R Package for Astrochronology [code], https://cran.r-project.org/package=astrochron (last access: July 2015), 2014.

Molnar, P., Boos, W. R., and Battisti, D. S.: Orographic controls on climate and paleoclimate of Asia: thermal and mechanical roles

for the Tibetan Plateau, Annu. Rev. Earth Pl. Sc., 38, 77–102, 2010.

Müller, D. W., Hodell, D. A., and Ciesielski, P. F.: 25. Late Miocene to earliest Pliocene (9.8–4.5 Ma) paleoceanography of the subantarctic southeast Atlantic: stable isotopic, sedimentologic, and microfossil evidence, in: Proc. ODP, College Station, TX (Ocean Drilling Program), edited by: Ciesielski, P. F., Kristoffersen, Y., Clement, B., and Moore, T. C., Scientific Results, 114, 459–474,1991.

Murray, R., Knowlton, C., Leinen, M., Mix, A. C., and Polsky, C.: Export production and carbonate dissolution in the central equatorial Pacific Ocean over the past 1 Myr, Paleoceanography, 15, 570–592, 2000.

Nigrini, C.: Composition and biostratigraphy of radiolarian assemblages from an area of upwelling (northwestern Arabian Sea, Leg 117), in: Proc. ODP, College Station, TX (Ocean Drilling Program), edited by: Emeis, K.-C., Meyers, P. A., Niitsuma, M., and Prell, W. L., Scientific Results, 117, 89–126, 1991.

Nomura, R.: Paleogene to Neogene deep-sea paleoceanography in the eastern Indian Ocean: benthic foraminifera from ODP Sites 747, 757 and 758, Micropaleontology, 41, 251–290, 1995.

Paillard, D.: The Plio-Pleistocene climatic evolution as a consequence of orbital forcing on the carbon cycle, Clim. Past, 13, 1259–1267, https://doi.org/10.5194/cp-13-1259-2017, 2017.

Pälike, H., Lyle, M. W., Nishi, H., Raffi, I., Ridgwell, A., Gamage, K., Klaus, A., Acton, G., Anderson, L., and Backman, J.: A Cenozoic record of the equatorial Pacific carbonate compensation depth, Nature, 488, 609–614, 2012.

Paytan, A. and Griffith, E. M.: Marine barite: Recorder of variations in ocean export productivity, Deep-Sea Res. Pt. II, 54, 687–705, 2007.

Paytan, A. and Kastner, M.: Benthic Ba fluxes in the central Equatorial Pacific, implications for the oceanic Ba cycle, Earth Planet. Sc. Lett., 142, 439–450, 1996.

Paytan, A., Kastner, M., Martin, E., Macdougall, J., and Herbert, T.: Marine barite as a monitor of seawater strontium isotope composition, Nature, 366, 445–449, 1993.

Paytan, A., Kastner, M., and Chavez, F.: Glacial to interglacial fluctuations in productivity in the equatorial Pacific as indicated by marine barite, Science, 274, 1355–1357, 1996.

Pickering, K. T., Carter, A., Andò, S., Garzanti, E., Limonta, M., Vezzoli, G., and Milliken, K. L.: Deciphering relationships between the Nicobar and Bengal submarine fans, Indian Ocean, Earth Planet. Sc. Lett., 544, 116329, https://doi.org/10.1016/j.epsl.2020.116329, 2020a.

Pickering, K. T., Pouderoux, H., McNeill, L. C., Backman, J., Chemale, F., Kutterolf, S., Milliken, K. L., Mukoyoshi, H., Henstock, T. J., and Stevens, D. E.: Sedimentology, stratigraphy and architecture of the Nicobar Fan (Bengal–Nicobar Fan System), Indian Ocean: Results from International Ocean Discovery Program Expedition 362, Sedimentology, 67, 2248–2281, 2020b.

Pierce, J., Weissel, J., Taylor, E., Dehn, J., Driscoll, N., Farrell, J., Fourtanier, E., Frey, F., Qamson, P. D., Gee, J. S., Gibson, I. L., Janecek, T., Klootwijk, C., Lawrence, J. R., Littke, R., Newman, J. S., Nomura, R., Owen, R. M., Pospichal, J. J., Rea, D. K., Resiwati, P., Saunders, A. D., Smit, J., Smith, G. M., Tamaki, K., Weis, D., and Wilkinson, C.: Proceedings of the Ocean Drilling Program, Initial Reports 121, 1000 pp., 1989.

Pimm, A.: Sedimentology and history of the northeastern Indian Ocean from late Cretaceous to Recent, in: Initial Reports of the Deep Sea Drilling Project, edited by: von der Borch, C. C., Sclater, J. G., Gartner Jr., S., Hekinian, R., Johnson, D. A., McGowran, B., Pimm, A. C., Thompson, R. W., Veevers, J. J., and Waterman, L. S., U.S. Government Printing Office, Washington, XXII, 717–803, https://doi.org/10.2973/dsdp.proc.22.139.1974, 1974.

Prasanna Kumar, S., Muraleedharan, P., Prasad, T., Gauns, M., Ramaiah, N., De Souza, S., Sardesai, S., and Madhupratap, M.: Why is the Bay of Bengal less productive during summer monsoon compared to the Arabian Sea?, Geophys. Res. Lett., 29, 88-81–88-84, 2002.

Prell, W. L. and Kutzbach, J. E.: Monsoon variability over the past 150,000 years, J. Geophys. Res.-Atmos., 92, 8411–8425, 1987.

Prell, W. L. and Kutzbach, J. E.: Sensitivity of the Indian monsoon to forcing parameters and implications for its evolution, Nature, 360, 647–652, 1992.

Privé, N. C. and Plumb, R. A.: Monsoon dynamics with interactive forcing. Part I: Axisymmetric studies, J. Atmos. Sci., 64, 1417–1430, 2007a.

Privé, N. C. and Plumb, R. A.: Monsoon dynamics with interactive forcing. Part II: Impact of eddies and asymmetric geometries, J. Atmos. Sci., 64, 1431–1442, 2007b.

Rae, J. W., Zhang, Y. G., Liu, X., Foster, G. L., Stoll, H. M., and Whiteford, R. D.: Atmospheric CO_2 over the Past 66 Million Years from Marine Archives, Annu. Rev. Earth Pl. Sc., 49, 609–641, 2021.

Ramaswamy, V.: Lithogenic Fluxes to the Northern Indian Ocean, Monsoon biogeochemistry, University of Hamburg, Germany, 1993.

Rial, J. A. and Anaclerio, C.: Understanding nonlinear responses of the climate system to orbital forcing, Quaternary Sci. Rev., 19, 1709–1722, 2000.

Rickaby, R., Bard, E., Sonzogni, C., Rostek, F., Beaufort, L., Barker, S., Rees, G., and Schrag, D.: Coccolith chemistry reveals secular variations in the global ocean carbon cycle?, Earth Planet. Sc. Lett., 253, 83–95, 2007.

Rixen, T., Gaye, B., Emeis, K.-C., and Ramaswamy, V.: The ballast effect of lithogenic matter and its influences on the carbon fluxes in the Indian Ocean, Biogeosciences, 16, 485–503, https://doi.org/10.5194/bg-16-485-2019, 2019.

Robinson, M. M., Bartol, M., Bolton, C. T., Ding, X., Gariboldi, K., Romero, O. E., and Expeditions 353 Scientists: Biostratigraphic Summary, in: Proceedings of the International Ocean Discovery Program Volume 353, https://doi.org/10.14379/iodp.proc.353.109.2016, 2016.

Rogalla, U. and Andruleit, H.: Precessional forcing of coccolithophore assemblages in the northern Arabian Sea: Implications for monsoonal dynamics during the last 200,000 years, Mar. Geol., 217, 31–48, 2005.

Rostek, F., Bard, E., Beaufort, L., Sonzogni, C., and Ganssen, G.: Sea surface temperature and productivity records for the past 240 kyr in the Arabian Sea, Deep-Sea Res. Pt. II, 44, 1461–1480, 1997.

Schmitz, B.: Barium, equatorial high productivity, and the northward wandering of the Indian continent, Paleoceanography, 2, 63–77, 1987.

Schott, F. A. and McCreary Jr., J. P.: The monsoon circulation of the Indian Ocean, Prog. Oceanogr., 51, 1–123, 2001.

Schott, F. A., Xie, S. P., and McCreary Jr., J. P.: Indian Ocean circulation and climate variability, Rev. Geophys., 47, RG1002, https://doi.org/10.1029/2007RG000245, 2009.

Sengupta, D., Bharath Raj, G., Ravichandran, M., Sree Lekha, J., and Papa, F.: Near-surface salinity and stratification in the north Bay of Bengal from moored observations, Geophys. Res. Lett., 43, 4448–4456, 2016.

Shackleton, N. J. and Hall, M. A.: The Late Miocene stable isotope record, Site 926, in: Proc. ODP, College Station, TX (Ocean Drilling Program), edited by: Shackleton, N. J., Curry, W. B., Richter, C., and Bralower, T. J., Scientific Results, 154, 367–373, 1997.

Shackleton, N. J., Hall, M., and Pate, D.: 15. Pliocene stable isotope stratigraphy of Site 846, in: Proc. ODP, College Station, TX (Ocean Drilling Program), edited by: Pisias, N. G., Mayer, L. A., Janecek, T. R., Palmer-Julson, A., and van Andel, T. H., Proceedings of the Ocean Drilling Program, Scientific Results, 138, 337–355, 1995.

Shimmield, G. B. and Mowbray, S. R.: The inorganic geochemical record of the northwest Arabian Sea: a history of productivity variation over the last 400 ky from Sites 722 and 724, in: Proc. ODP, College Station, TX (Ocean Drilling Program), edited by: Emeis, K.-C., Meyers, P. A., Niitsuma, M., and Prell, W. L., Proceedings of the Ocean Drilling Program, Scientific Results, 117, 409–429, 1991.

Shipboard Scientific Party: Site 758, in: Proceedings of ODP, College Station, TX, edited by: Peirce, J., Weissel, J., Taylor, E., and Shipboard Scientists, Proceedings of the Ocean Drilling Program, Initial Reports, 121, 359–453, 1989.

Si, W. and Rosenthal, Y.: Reduced continental weathering and marine calcification linked to late Neogene decline in atmospheric CO_2, Nat. Geosci., 12, 833–838, 2019.

Singh, A. D., Jung, S. J., Darling, K., Ganeshram, R., Ivanochko, T., and Kroon, D.: Productivity collapses in the Arabian Sea during glacial cold phases, Paleoceanography, 26, PA3210, https://doi.org/10.1029/2009PA001923, 2011.

Singh, R. K. and Gupta, A.: Miocene history of Indian monsoon: A review of marine records, in: Indian Miocene: A Geodynamic and chronologic framework for palaeobiota, sedimentary environments and palaeoclimates, edited by: Tiwari, R. P., Special Publication of the Palaeontological Society of India, 5, 101–109, 2014.

Smart, C. W., Thomas, E., and Ramsay, A. T.: Middle–late Miocene benthic foraminifera in a western equatorial Indian Ocean depth transect: paleoceanographic implications, Palaeogeogr. Palaeocl., 247, 402–420, 2007.

Spicer, R., Yang, J., Herman, A., Kodrul, T., Aleksandrova, G., Maslova, N., Spicer, T., Ding, L., Xu, Q., and Shukla, A.: Paleogene monsoons across India and South China: Drivers of biotic change, Gondwana Res., 49, 350–363, 2017.

Steinthorsdottir, M., Coxall, H., de Boer, A., Huber, M., Barbolini, N., Bradshaw, C., Burls, N., Feakins, S., Gasson, E., and Henderiks, J.: The Miocene: the Future of the Past, Paleoceanography and Paleoclimatology, 36, e2020PA004037, https://doi.org/10.1029/2020PA004037, 2021.

Stow, D. A., Amano, K., Batson, B., Brass, G. W., Corrigan, J., Raman, C., Tiercelin, J.-J., Townsend, M., Wijayananda, N., and Cochran, J.: Sediment facies and processes on the distal Bengal Fan, Leg 116, in: Proc. ODP, College Station, TX (Ocean Drilling Program), edited by: Cochran, J. R., Stow, D. A. V., and Expedition 116 Scientists, Proceeding of the Ocean Drilling Program, Scientific Results, 116, 377–396, 1990.

Sun, J. and Huang, X.: Half-precessional cycles recorded in Chinese loess: response to low-latitude insolation forcing during the Last Interglaciation, Quaternary Sci. Rev., 25, 1065–1072, 2006.

Sun, X. and Wang, P.: How old is the Asian monsoon system? – Palaeobotanical records from China, Palaeogeogr. Palaeocl., 222, 181–222, 2005.

Tabor, C. R., Otto-Bliesner, B. L., Brady, E. C., Nusbaumer, J., Zhu, J., Erb, M. P., Wong, T. E., Liu, Z., and Noone, D.: Interpreting precession-driven $\delta^{18}O$ variability in the South Asian monsoon region, J. Geophys. Res.-Atmos., 123, 5927–5946, 2018.

Tauxe, L. and Feakins, S.: A re-assessment of the chronostratigraphy of late Miocene C_3–C_4 transitions, Paleoceanography and Paleoclimatology, 35, e2020PA003857, https://doi.org/10.1029/2020PA003857, 2020.

Thomas, E. K., Clemens, S. C., Sun, Y., Prell, W. L., Huang, Y., Gao, L., Loomis, S., Chen, G., and Liu, Z.: Heterodynes dominate precipitation isotopes in the East Asian monsoon region, reflecting interaction of multiple climate factors, Earth Planet. Sc. Lett., 455, 196–206, 2016.

Tripathi, S., Tiwari, M., Lee, J., Khim, B.-K., Expedition, I., Pandey, D. K., Clift, P. D., Kulhanek, D. K., Andò, S., and Bendle, J. A.: First evidence of denitrification vis-à-vis monsoon in the Arabian Sea since Late Miocene, Scientific Reports, 7, 43056, https://doi.org/10.1038/srep43056, 2017.

Unger, D. and Jennerjahn, T.: Impact of regional Indian Ocean characteristics on the biogeochemical variability of settling particles, in: Indian Ocean Biogeochemical Processes and Ecological Variability, Geophysical Monograph Series, 185, 257–280, https://doi.org/10.1029/2008GM000703, 2009.

Unger, D., Ittekkot, V., Schäfer, P., Tiemann, J., and Reschke, S.: Seasonality and interannual variability of particle fluxes to the deep Bay of Bengal: influence of riverine input and oceanographic processes, Deep-Sea Res. Pt. II, 50, 897–923, 2003.

Van Andel, T. H., Heath, G. R., and Moore Jr., T. C.: Cenozoic History and Paleoceanography of the Central Equatorial Pacific Ocean: A Regional Synthesis of Deep Sea Drilling Project Data, The Geological Society of America, https://doi.org/https://doi.org/10.1130/MEM143-p1, 1975.

Vidya, P. J., Prasanna Kumar, S., Gauns, M., Verenkar, A., Unger, D., and Ramaswamy, V.: Influence of physical and biological processes on the seasonal cycle of biogenic flux in the equatorial Indian Ocean, Biogeosciences, 10, 7493–7507, https://doi.org/10.5194/bg-10-7493-2013, 2013.

Vinayachandran, P., Chauhan, P., Mohan, M., and Nayak, S.: Biological response of the sea around Sri Lanka to summer monsoon, Geophys. Res. Lett., 31, L01302, https://doi.org/10.1029/2003GL018533, 2004.

Wan, S., Li, A., Clift, P. D., and Stuut, J.-B. W.: Development of the East Asian monsoon: mineralogical and sedimentologic records in the northern South China Sea since 20 Ma, Palaeogeogr. Palaeocl., 254, 561–582, 2007.

Wang, P., Clemens, S., Beaufort, L., Braconnot, P., Ganssen, G., Jian, Z., Kershaw, P., and Sarnthein, M.: Evolution and variability

of the Asian monsoon system: state of the art and outstanding issues, Quaternary Sci. Rev., 24, 595–629, 2005.

Wang, P., Tian, J., and Lourens, L. J.: Obscuring of long eccentricity cyclicity in Pleistocene oceanic carbon isotope records, Earth Planet. Sc. Lett., 290, 319–330, https://doi.org/10.1016/j.epsl.2009.12.028, 2010.

Webber, B. G., Matthews, A. J., Vinayachandran, P., Neema, C., Sanchez-Franks, A., Vijith, V., Amol, P., and Baranowski, D. B.: The dynamics of the Southwest Monsoon current in 2016 from high-resolution in situ observations and models, J. Phys. Oceanogr., 48, 2259–2282, 2018.

Webster, P. J.: The elementary monsoon, in: Monsoons, edited by: Fein, J. S. and Stephens, P. L., Wiley, New York, 3–32, 1987a.

Webster, P. J.: The variable and interactive monsoon, in: Monsoons, edited by: Fein, J. S. and Stephens, P. L., John Wiley, New York, 269–330, 1987b.

Webster, P. J. and Yang, S.: Monsoon and ENSO: Selectively interactive systems, Q. J. Roy. Meteor. Soc., 118, 877–926, 1992.

Westerhold, T., Marwan, N., Drury, A. J., Liebrand, D., Agnini, C., Anagnostou, E., Barnet, J. S., Bohaty, S. M., De Vleeschouwer, D., and Florindo, F.: An astronomically dated record of Earth's climate and its predictability over the last 66 million years, Science, 369, 1383–1387, 2020.

Zeeden, C., Hilgen, F., Westerhold, T., Lourens, L., Röhl, U., and Bickert, T.: Revised Miocene splice, astronomical tuning and calcareous plankton biochronology of ODP Site 926 between 5 and 14.4 Ma, Palaeogeogr. Palaeocl., 369, 430–451, 2013.

Zeeden, C., Hilgen, F. J., Hüsing, S. K., and Lourens, L. L.: The Miocene astronomical time scale 9–12 Ma: New constraints on tidal dissipation and their implications for paleoclimatic investigations, Paleoceanography, 29, 296–307, 2014.

Zeeden, C., Meyers, S. R., Lourens, L. J., and Hilgen, F. J.: Testing astronomically tuned age models, Paleoceanography, 30, 369–383, 2015.

Zhisheng, A., Clemens, S. C., Shen, J., Qiang, X., Jin, Z., Sun, Y., Prell, W. L., Luo, J., Wang, S., and Xu, H.: Glacial-interglacial Indian summer monsoon dynamics, Science, 333, 719–723, 2011.

Zhuang, G., Pagani, M., and Zhang, Y. G.: Monsoonal upwelling in the western Arabian Sea since the middle Miocene, Geology, 45, 655–658, 2017.

Ziegler, M., Lourens, L. J., Tuenter, E., Hilgen, F., Reichart, G. J., and Weber, N.: Precession phasing offset between Indian summer monsoon and Arabian Sea productivity linked to changes in Atlantic overturning circulation, Paleoceanography, 25, PA3213, https://doi.org/10.1029/2009PA001884, 2010.

Zweng, M., Reagan, J., Antonov, J., Locarnini, R., Mishonov, A., Boyer, T., Garcia, H., Baranova, O., Johnson, D., and Seidov, D.: World Ocean Atlas 2013, Volume 2: Salinity, edited by: Levitus, S. and Mishonov, A., NOAA Atlas NESDIS 74, 39 pp., 2013.